Gill, A. E. 1971. The equatorial current in a homogeneous ocean. Deep Sea Res., *18,* 421–431.
—— 1975. Models of equatorial currents, *in* Proc. Symp. on Numerical Models of Ocean Circulation, Washington, D.C., Nat. Acad. Sci., 364 p.
Knauss, J. A. 1966. Further measurements and observations on the Cromwell Current. J. Mar. Res., *24,* 205–240.
Knox, R. A. 1976. On a long series of measurements of Indian Ocean equatorial currents near Addu Atoll. Deep Sea Res., *23,* 211–221.
Leetmaa, A. 1973. The response of the Somali Current at 2°S to the southwest monsoon of 1971. Deep Sea Res., *20,* 397–400.
Lighthill, M. J. 1969. Dynamic response of the Indian Ocean to onset of the southwest monsoon. Phil. Trans., Roy. Soc., *A 265,* 45–92.
Matsuno, T. 1966. Quasi geostrophic motions in the equatorial area. J. Met. Soc. Japan, *44,* 25–43.
McKee, W. D. 1973. The wind-driven equatorial circulation in a homogeneous ocean. Deep Sea Res., *20,* 889–899.
Munk, W. H. 1950. On the wind-driven ocean circulation. J. Meteorol., *7,* 79–93.
O'Brien, J. J. and H. E. Hurlbut. 1974. An equatorial jet in the Indian Ocean, Theory. Science, *184,* 1075–1077.
Pedlosky, J., 1968. An overlooked aspect of the wind-driven ocean circulation. J. Fluid Mech., *32,* 809–821.
Philander, S. G. H. 1971. The equatorial dynamics of a shallow homogeneous ocean. Geophys. Fluid Dyn., *2,* 219–245.
—— 1973a. The equatorial thermocline. Deep Sea Res., *20,* 69–86.
—— 1973b. Equatorial undercurrent: measurements and theories. Rev. Geophys., *11,* 513–570.
—— 1976. Instabilities of zonal equatorial currents. J. Geophys. Res., *81,* 3725–3735.
—— 1978. Forced oceanic waves. Rev. Geophys. Space Phys., *16,* 15–46.
Robinson, A. R. 1960. The general thermal circulation in the equatorial regions. Deep Sea Res., *6,* 311–317.
—— 1966. An investigation into the wind as the cause of the Equatorial Undercurrent. J. Mar. Res., *24,* 179–204.
—— 1970. Boundary layers in ocean circulation models in Annual Review of Fluid Mechanics *2,* Palo Alto, Annual Reviews Inc., 312 pp.
Stommel, H. 1948. The westward intensification of wind-driven currents. Trans. Amer. Geophys. Union, *29,* 202–206.
—— 1960. Wind-drift near the equator. Deep Sea Res., *6,* 298–302.
Sverdrup, H. D. 1947. Wind-driven currents in a baroclinic ocean, with applications to the equatorial currents of the eastern Pacific. Proc. Nat'l. Acad. Sci., *33,* 318–326.
Taft, B., B. Hickey, C. Wunsch and D. Baker. 1974. The Cromwell Current at 150°W. Deep Sea Res., *21,* 403–430.
Veronis, G. 1963a. On the approximations involved in transforming the equations of motion from a spherical to the β-Plane, part I. Barotropic systems, J. Mar. Res., *21,* 110–124.
—— 1963b. On the approximations involved in transforming the equations of motion from a spherical to the β-Plane, part II. Baroclinic systems, J. Mar. Res., *21,* 199–204.
Veronis, G. and H. Stommel. 1956. The action of variable wind stresses on a stratified ocean, J. Mar. Res., *15,* 43–75.
Williams, R. and C. Gibson. 1974. Direct measurement of turbulence in the Pacific Equatorial Undercurrent. J. Phys. Oceanogr., *4,* 104–108.

Received: *27 June, 1977;* revised: *22 November, 1978.*

The response of an equatorial ocean to simple wind stress patterns: II. Numerical results

by Mark A. Cane[1]

ABSTRACT

The model developed by Cane (1978) is used to study the wind-driven circulation in an equatorial ocean. Simple wind stress patterns are imposed and the model evolution and eventual steady state are calculated numerically. Both linear and fully nonlinear responses are discussed; dynamical arguments are presented to account for the principal features.

The setup time in the model experiments was on the order of several hundred days, with the implication that none of the world's equatorial oceans is in equilibrium with the seasonally varying winds. The Atlantic and Indian Oceans will be close to this equilibrium state while the wider Pacific will not. Nonlinear effects become significant within two weeks. Depending on the form of the wind stress, the inclusion of nonlinearities may either lengthen or shorten the corresponding linear spin up time.

The nonlinear responses to zonal winds included a strong eastward equatorial undercurrent, in agreement with observations. Other aspects of the flow qualitatively resemble the linear response and are largely explicable in terms of wave dynamics. With easterlies, the undercurrent requires a basin-wide zonal pressure gradient: the dynamics are nonlocal and the undercurrent takes several months to reach full strength. With westerlies (as in the Indian Ocean) the subsurface eastward flow is caused by frictional-inertial dynamics that are local and rapid: this undercurrent reaches full strength within one week, consistent with observations at Gan (Knox, 1976).

The nonlinear response to a southerly wind stress is inertially determined and wave concepts are inapplicable. There is an intense eastward "countercurrent" at 3N, entirely independent of the wind stress curl. The zonal mean state is barotropically unstable and westward propagating waves appear. With southeasterlies there is an eastward jet at 4N and undercurrent shifts south of the equator, meandering with longitude. The purely zonal wind cases are stable, suggesting that observed instabilities are due to the equatorial current system as a whole and not the undercurrent itself. Additional theoretical and observational implications of these results are discussed.

1. Introduction

In this paper the response of a bounded equatorial ocean to an imposed wind stress is studied. It is an extension of previous investigations (especially Charney and

1. NASA/Goddard Space Flight Center, Laboratory for Atmospheric Sciences, Greenbelt, Maryland, 20771, U.S.A.

Table 1. Standard values of model parameters.

Parameter	Value	Remarks
τ	.465 dyn cm^{-2}/(gm cm^{-3})	Wind stress per unit mass
g'	.1724 msec^{-2}	"reduced gravity" $g' = g\,(\rho_2-\rho_1)/\rho_2$ for $(\rho_2-\rho_1)/\rho_2 = 1.76 \times 10^{-2}$
ν_H	5.86×10^5 cm^2 sec^{-1}	coefficient of horizontal viscosity
ν_v	15 cm^2 sec^{-1}	coefficient of vertical viscosity
K	1.5×10^{-3} msec^{-1}	interfacial friction parameter; $K = \nu_v/H^*$ for $H^* = 100$ m
K_B	1.5×10^{-6} msec^{-1}	bottom friction parameter; $K_B = K$
X_B	28.6° (3184 km)	zonal extent of the basin
θ_T	15°	basin walls are at 15N and 15S
θ_B	−15°	
η	25 m	depth of upper layer
$\bar{H}_1$	175 m	mean value of the lower layer depth h
β	2.2×10^{-11}m^{-1}sec^{-1}	$\beta = (df/dy)_{y=0} = 2\Omega/R$ where $\Omega = 2\pi$ day^{-1} and R is the radius of the earth

Spiegel, 1971) to include zonal variations of the oceanic currents as well as time dependence. The intent is to experiment with a laboratory-like model to gain some insight into equatorial dynamics. We do not attempt to achieve a close mimicry of the real ocean. The linear dynamics were explored rather thoroughly by analytic methods in Cane (1979), henceforth referred to as I. Here we will report on numerical calculations of both the linear and the fully nonlinear responses. Comparisons will be made with the analytic results of I and additional simple analytic models will be invoked to explain some of the phenomena observed in the computations.

The remainder of this section is a brief account of the physical model, while Sec. 2 describes the numerical methods used to obtain solutions. The six sections that follow present the results of experiments with simple wind stress patterns. The final section discusses the implications of these results for the world's oceans.

The physical model. The physical model was formulated in I. That paper also has a lengthy discussion of the choice of values for the governing physical parameters; the results are summarized in Table 1. The model is time dependent and treats fully variations in both the zonal and meridional directions. The vertical structure consists of two layers above the thermocline with the same constant density (Fig. 1). The ocean below the thermocline is taken to be of a higher constant density and to be approximately at rest. The upper of the two active layers is a constant depth surface layer which is acted upon directly by the wind stress. The lower active layer is not directly affected by the wind. Its depth is variable, with the variations being dynamically determined. The two layers communicate via the vertical velocity at their interface, as well as frictionally. Extra-equatorially, this structure is equivalent

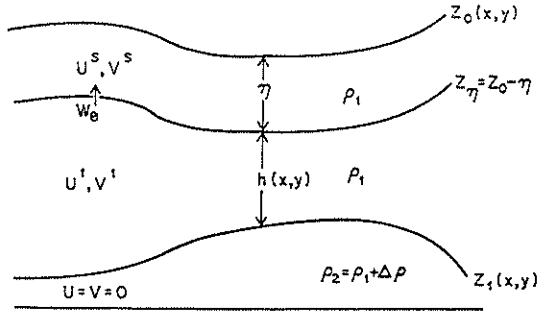

Figure 1. Two layer model.

to a surface Ekman layer and an interior in which the currents are in geostrophic balance.

The layer configuration described above allows for the vertical inhomogeneity that results from the wind stress being felt directly by the ocean at the surface but only indirectly below (e.g., via boundary layer pumping). If the wind stress has no curl, the more usual layered model with each layer having a different density (e.g., Charney, 1955) admits a steady state solution in which each interface tilts in such a way that there is no motion in any of the layers. The present model has the simplest vertical structure that permits a steady state undercurrent.

As in I the equations are nondimensionalized to facilitate our analysis. Letting $\bar{H} = \bar{H}_1 + \eta$, $L = (g'\bar{H}/\beta^2)^{1/4}$, $T = (\beta L)^{-1}$ and $U = \tau_0(\bar{H}\beta L)^{-1}$ we scale the variables as follows:

$$(x,y) = L(x'y'), \qquad (\mathbf{u}^s,\mathbf{u}^1) = U(\mathbf{u}^{s\prime},\mathbf{u}^{1\prime}),$$
$$\eta = \bar{H}\alpha, \qquad w_e = [U\bar{H}/L]w_e',$$
$$h = \bar{H}_1 + [U\beta L^2/g']h', \qquad \tau = \tau_0\tau'$$
$$t = Tt',$$

Dropping the primes the governing eqations become (cf. I):

$$\mathbf{u}_t^s + \epsilon\{(\mathbf{u}^s \cdot \nabla)\,\mathbf{u}^s + \frac{w_e}{2\alpha}(\mathbf{u}^s - \mathbf{u}^1)\} + y\,\mathbf{k} \times \mathbf{u}^s$$
$$= -\nabla h + \boldsymbol{\tau}/\alpha + A\,\nabla^2\mathbf{u}^s - (1-\alpha)\,\gamma_I\,(\mathbf{u}^s - \mathbf{u}^1)\,; \tag{1.1a}$$

$$\mathbf{u}_t^1 + \epsilon\left\{(\mathbf{u}^1 \cdot \nabla)\,\mathbf{u}^1 + \frac{w_e\,(\mathbf{u}^s - \mathbf{u}^1)}{2(1-\alpha+\epsilon h)}\right\} + y\,\mathbf{k} \times \mathbf{u}^1$$
$$= -\nabla h + A\,\nabla^2\mathbf{u}^1 + \alpha\,\gamma_I\,(\mathbf{u}^s - \mathbf{u}^1)\left[\frac{1-\alpha}{1-\alpha+\epsilon h}\right] - \frac{\gamma\mathbf{u}^1}{1-\alpha+\epsilon h}\,; \tag{1.1b}$$

$$w_e = \alpha \nabla \cdot \mathbf{u}^s ; \tag{1.1c}$$

$$h_t + (1-\alpha) \nabla \cdot \mathbf{u}^1 + \alpha \nabla \cdot \mathbf{u}^s + \epsilon \nabla \cdot (h\mathbf{u}^1) = 0 . \tag{1.1d}$$

where the following nondimensional numbers have been introduced:

Rossby number	$\epsilon = U/(\beta L^2)$;
Horizontal Ekman number	$A = \nu_H/(\beta L^3)$;
Interfacial Ekman number	$\gamma_I = K/(\beta L \bar{H} \alpha[1-\alpha])$;
Bottom Ekman number	$\gamma = K_B/(\beta L \bar{H})$;
Nondimensional boundary layer depth	$\alpha = \eta/\bar{H}$.

The boundary conditions are that at all lateral boundaries $\mathbf{u}^s = \mathbf{u}^1 = 0$. The parameters are chosen so that the vertical eddy exchanges dominate the horizontal ones. However, as discussed in I, the horizontal eddy viscosity must be nonzero to allow these boundary conditions to be imposed.

Some of the symbols appearing above are defined in Table 1 or Figure 1; the others follow standard oceanographic usage. The model ocean is taken to be on an equatorial β-plane so that the Coriolis parameter is given by $f = \beta y$. Eastward and northward distances are given by the Cartesian coordinates x and y, respectively, with the origin of the coordinate system at the intersection of the equator with the western boundary. The operators ∇ and ∇^2 have their usual two dimensional meanings. The surface layer velocity $\mathbf{u}^s$ has components u^s in the eastward and v^s in the northward direction. Similarly, the velocity of the lower layer, $\mathbf{u}^1 = (u^1, v^1)$. Note that w_e is the surface layer suction: i.e., the rate of exchange between the layers of volume per unit area. This is not the same as the vertical velocity at the interface, $w(z_\eta) \equiv dz_\eta/dt$.

It will prove useful to introduce two quantities defined in I:

$$\tilde{\mathbf{u}} = \alpha \mathbf{u}^s + [1-\alpha+\epsilon h]\, \mathbf{u}^1 ; \; \tilde{\mathbf{u}} = \alpha\, (\mathbf{u}^s - \mathbf{u}^1); \tag{1.3}$$

where $\tilde{\mathbf{u}}$ is the *vertically integrated transport* and $\tilde{\mathbf{u}}$ is the frictional boundary layer transport (see I). In mid-latitudes $\tilde{\mathbf{u}}$ is the Ekman layer transport. Eqs. (1.1) may be linearized about a resting basic state with a mean lower layer depth H_1 (i.e., $h = \mathbf{u}^s = \mathbf{u}^1 = 0$) by setting $\epsilon \equiv 0$. Then it was shown in I that the governing equations for $\tilde{\mathbf{u}}$ and h are just the linear shallow water equations driven by the wind stress τ. A method for solving the time dependent, inviscid version of these equations has been given by Cane and Sarachik (1976, 1977, 1979) henceforth CSI, CSII and CSIII. The growth of $\tilde{\mathbf{u}}$ results from the wind driving $\boldsymbol{\tau}$ and is limited by Coriolis effects extra-equatorially and by the interfacial friction near the equator (see I).

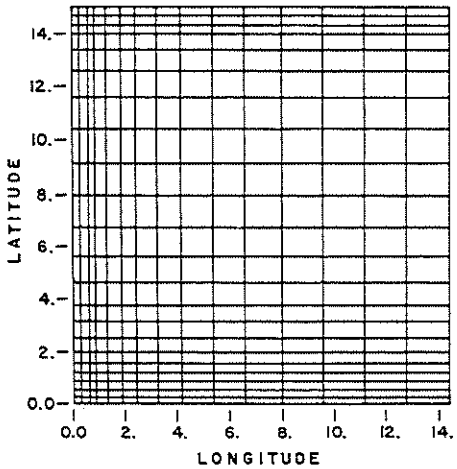

Figure 2. Grid configuration. Only ¼ of the full grid is shown; the grid is symmetric about the equator and the longitude $x = 14.3°$. In this and subsequent figures latitude and longitude are given in degrees (1 degree = 111 km.)

2. Numerical methods

The methods used for the numerical solutions of (1.1) are described in detail in Cane (1975). The salient features will be discussed briefly here.

a. Grid configuration. An unstaggered variable size grid mesh is employed to allow increased resolution for the sidewall boundary layers and along the equator. The grid points are shown in Figure 2. Following a suggestion of M. Israeli (Orszag and Israeli, 1974) the location x_i of the ith point in physical space is determined by solving an equation of the form

$$x_i^* = a + bx_i + \sum_j \alpha_j \tan^{-1} [\beta_j^{-1} (x_i - \gamma_j)] \tag{2.1}$$

so that the points x_i^* in the "computational space" are equally spaced; i.e. (2.1) is solved for the x_i that gives $x_i^* = (i-1)\Delta x$. Many of the figures (e.g. Fig. 6) are plotted in the computation coordinate x^* rather than the physical coordinate x in order to increase the visual area devoted to regions of interest (e.g. the equator). In (2.1) β_j is (a measure of) the thickness of the boundary layer at $x = \gamma_j$ and α_j is a weighting factor determining how many mesh points will be in this boundary layer.

b. Time differencing. Time marching is accomplished with the N-cycle scheme of Lorenz (1971) with $N = 4$. This scheme is second order in time (fourth order for linear equations). In the calculations reported here we use a timestep of $(4\Omega)^{-1} \approx$ 1 hour.

c. Spatial differencing. All derivatives are approximated by centered fourth order finite differences in the interior and by third order differences at the points on and immediately adjacent to the boundary. Since the spacing at the boundary is smaller than in the interior, this does not degrade the overall accuracy. The finite difference approximation D is made in the computational space where the grid points x_i^* are equally spaced. D may be related to the desired derivative $\partial f/\partial x$ in the physical space by

$$\frac{\partial f}{\partial x} = \frac{dx^*}{dx}\frac{\partial f}{\partial x^*} \approx \frac{dx^*}{dx} Df$$

where dx^*/dx is calculated (analytically) from (2.1).

The equations are differenced in a conservation form; that is, the spatial differencing is such that in the absence of sources and sinks momentum, energy and mass would be conserved. The exception to this is that the treatment of boundary points does not identically conserve these properties. Tests showed the leakage of mass and energy at the boundaries to be negligibly small (the order of computational round-off errors).

d. Gravity wave treatment; smoothing. The use of conservation forms does not prevent short wave length computational modes (e.g. "checkerboard instabilities") from growing to noticeable size. Physically, one expect gravity waves to adjust the flow to a more slowly varying (e.g. geostrophic) balance by propagating away such small scale disturbances. Mesinger (1972) has pointed out that the usual numerical treatments of gravity waves fails to couple the grid points properly. This accounts for the disparity between their physical and numerical roles.

The simplest set of linear equations describing gravity waves is

$$u_t = -g\frac{\partial}{\partial x}h; \quad h_t = -H\frac{\partial}{\partial x}u\,. \tag{2.2}$$

The finite difference analog is obtained by replacing $\partial/\partial x$ by a finite difference approximation D_x:

$$u_t = -gD_x h; \quad h_t = -HD_x u\,. \tag{2.3}$$

From (2.2) a single equation in h is readily derived:

$$h_{tt} = gHh_{xx} \tag{2.4}$$

The analog obtainable from (2.3) is

$$h_{tt} = gHD_x(D_x h)\,. \tag{2.5}$$

Note that the second derivative in (2.4) has been replaced by two successive first derivative approximations D_x^2 instead of a second derivative approximation D_{xx}. For second order centered differences and a two grid point wave, $h_i \equiv h(x_i) = (-1)^i$, the right-hand side of (2.5) is zero, so that (2.5) fails to propagate the wave. On the other hand $D_{xx}h_i = -4\Delta x^{-2}h_i \neq 0$.

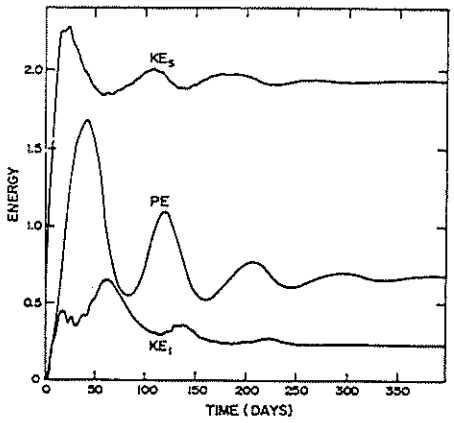

Figure 3. Evolution of energies in the linear response to an easterly wind. Potential energy (PE), and kinetic energy in the surface layer (KE_s) and lower layer (KE_1) for the equatorial region (5.6S to 5.6N) are shown. The unit of energy is $10^2\ Jm^{-2}R^2$, where R = 6367 km is the radius of the earth.

Our method of treating gravity waves amounts to replacing the D_x^2 operator in (2.5) with D_{xx} in order to retain the proper coupling between successive mesh points. (The implementation is straightforward but the details are lengthy and will be omitted here; see Cane, 1975, Appendix B.) Equivalently, it amounts to adding a smoother $S_x \equiv gH(D_{xx}-D_x^2)$. Since D_{xx} and D_x are the 4th order so is S_x and the formal order of accuracy of the equations is unchanged. Gravity waves in two dimensions require adding operators S_x to the u, S_y to the v and S_x and S_y to the h equations. In addition, it was necessary to add smoothers in the cross stream direction (i.e. S_y to the u and S_x to the v equations) because the horizontal viscosity used in the computations is too small to suppress two-grid point waves where the mesh spacing is large.

3. Linear response to a uniform easterly wind

The model equations are linearized by setting $\epsilon = 0$ in Eqs. (1.1); all model parameter values are as given in Table 1 with a uniform easterly wind stress switched on at $t = 0$. The linear dynamics may be understood rather thoroughly in terms of the analytic results in I and CSI, II, III. [CSIII, Sec. 5 has a detailed account of the early stages of spinup for the shallow water equations.] We present the linear numerical results here for the considerable light they shed on the nonlinear dynamics to be discussed in the following sections; our discussion will be focused accordingly.

The surface flow $\mathbf{u}^s$ is approximated well by the boundary layer velocity $\tilde{\mathbf{u}}$ [see (1.3)]. The latter evolves to a steady state on the frictional timescale of 20 days (see Fig. 3). Extra-equatorially, it approaches the Ekman wind drift solution; flow

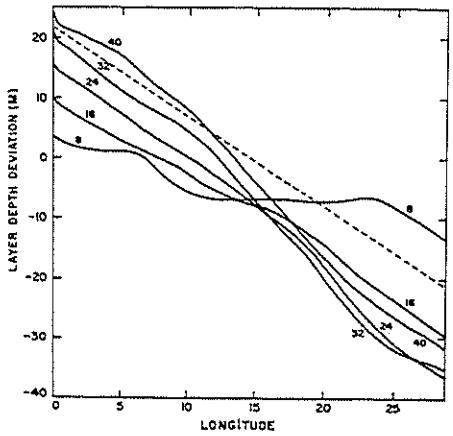

Figure 4. Sections of layer depth deviation, h, along the equator at 8 day intervals in the linear response to an east wind. Each solid curve is labelled with the time in days. The dashed line is the steady inviscid solution (3.2).

is poleward in both hemispheres, resulting in intense upwelling at the equator. Right on the equator the flow is westward, in the direction of the wind, with the turning from westward to poleward occurring within a degree of the equator in a boundary layer in which interfacial friction (γ_I) is important. Figure 3 shows that the lower layer currents are much weaker than those in the surface layer. The linearized dynamics do not allow vertical advection of momentum and the frictional and pressure forces are not capable of generating strong currents.

The time dependent solution for the vertically integrated transports and the layer depth h may be found by the methods of CSI,II. It has $\bar{u}$ and h symmetric and $\bar{v}$ antisymmetric about the equator. In the absence of boundaries, this part of the model response would consist of inertia-gravity waves together with functions of the form

$$(\bar{u},\bar{v},h) = (U(y)t,\ V(y),\ H(y)t) \tag{3.1}$$

(These functions are depicted in CSI Figure 8a for the wind stress $\tau^{(x)} = 1$, which is just the negative of the present case.) U and H are equatorially confined, while V goes to zero at the equator and approaches $-\tau^{(x)}/y$ as y increases. Most of the energy put in by the wind goes into (3.1); relatively little goes into the inertia-gravity waves.

We anticipate that (with the exception of the frictional equatorial boundary layer described in I and discussed further below) the final state will be one in which there is no motion and the surface tilts up uniformly from east to west to balance the wind stress:

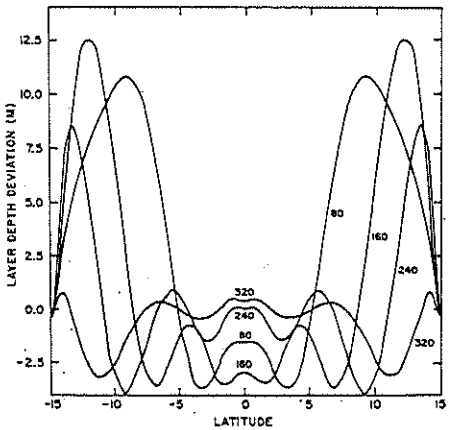

Figure 5. Sections of layer depth deviation, h, along the central longitude $x' = 14.3°$ at 80 day intervals in the linear response to an easterly wind. Labels give the time in days.

$$\bar{u} = \bar{v} = 0; \quad h = (x - X_E/2)\,\tau^{(x)}\ . \tag{3.2}$$

The adjustment to a final state will be accomplished by the boundary effects on the secularly growing part of (3.1). [See CSII and CSIII for a detailed discussion.] Both the eastern and western boundaries participate actively in the adjustment process because the presence of the eastward travelling Kelvin mode makes it impossible for the adjustment to proceed solely from the east. (Sec. 6 offers a contrasting case.) The Kelvin wave has negligible amplitude extra-equatorially, influencing that region only via the modes generated when it is reflected at the eastern end of the equator. Hence, all the extra-equatorial adjustment proceeds from east to west. The more equatorially confined modes travel the most rapidly so the equatorial region adjusts more rapidly.

The final state is not approached monotonically; for example, the gradient of h tends to "overshoot" its final value. This is evident in the energy curves (Fig. 3) with the most striking oscillations occurring in the potential energy. These oscillations are related to the reflections from the basin walls described in CSII. That analysis shows that the adjustment should have a periodicity of $4T$, where T is the time for a Kelvin wave to cross the basin. The additional $3T$ is the crossing time for the $n = 1$ Rossby wave generated by the Kelvin wave at the eastern boundary. Dimensionally T is 19.8 days so the predicted $4T$ periodicity is in excellent agreement with the 80 period observed in Figure 3.

Figure 4 shows profiles of the layer depth at the equator at various times. If the height were set up to balance the wind stress (3.2), the layer depth profile would be a straight line 21.8 m below (above) the mean value at the eastern (western) side (the dashed line in Fig. 4). During the course of the adjustment the profile tends to

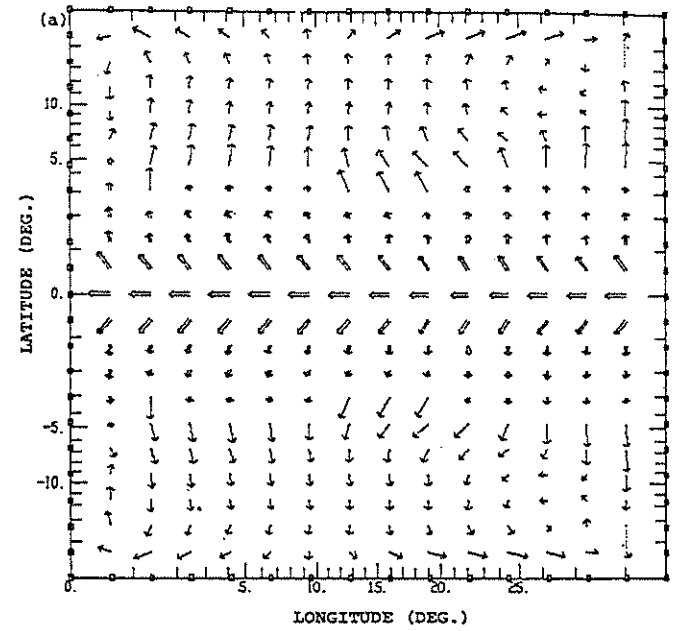

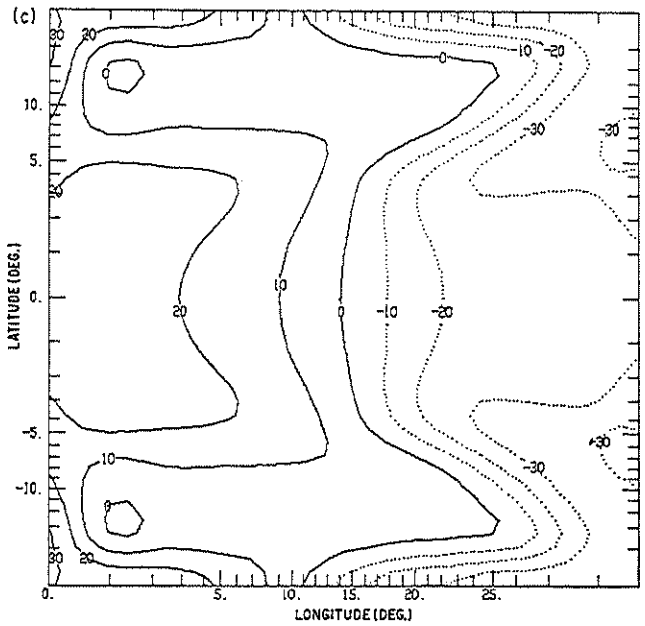

Figure 6. Linear response to an easterly wind at day 40. Note that the coordinates are stretched. (a) Surface layer velocity, $\mathbf{u}^1$. Dotted arrows: 0-2 cm s^{-1}; full arrows: 2-20 cm s^{-1}; double arrows: 20-200 cm s^{-1}. (b) Lower layer velocity, $\mathbf{u}^2$. (c) Layer depth deviation, h. Contour interval is 10 m.

be below this final value everywhere. The profile at 8 days shows a flat center section in which the boundary influences have not been felt; here h is decreasing in accordance with the unbounded solution (3.1). At this time, the Kelvin mode generated at the western boundary has propagated 12° into the basin. This is evident in the sloping region at the western side of the basin. Near $x = 0$ there is also evidence of the effect of the boundary trapped modes. At the eastern side there is another sloping piece to the profile extending 4° into the basin. This is due to the Rossby modes generated at the boundary; the fastest of these (the one with meridional index $n = 1$) would have propagated 4° at this time.

At 15 days the two boundary influences meet at a point three-quarters of the way across the basin. Until this time, the magnitude of the westward zonal transport at this point has increased according to (3.1). Hereafter the slope of the height field at all longitudes on the equator will be up toward the west, thus reducing the zonal acceleration. In fact, it is evident from Figure 4 that by 24 days this gradient is generally sufficient to balance the wind stress so that the magnitude of the westward transport will no longer increase. The slopes at the eastern side become steeper than what is required to balance the wind stress so that the transport here becomes

eastward and the layer deepens. This region of eastward flow is behind the front formed by the Rossby modes which are the reflections of the first Kelvin mode to cross the basin. The region propagates out from the eastern boundary beginning at day 20.

Consideration of the zonal transports at the equator indicates that the *equatorial region* takes approximately 250 days to approach its final steady state; this time scale agrees with the energy diagram, Figure 3. At each longitude the steady state layer depth profile is a straight line independent of latitude [cf. (3.2)]. At all longitudes this is attained more rapidly close to the equator. Near the eastern wall h is close to its steady value at all latitudes after 300 days. At the center of the basin the profile still shows some deviation from the expected final value $h = 0$ poleward of about 7° (Fig. 5). There is a strong tilt at the northern and southern walls to geostrophically balance the boundary jets present there [cf. CSIII]. Profiles near the western boundary are even further from their steady state values. As was previously mentioned, analytic theory predicts that the pattern of adjustment will be from east to west and from the equator poleward.

At 40 days (Fig. 6) the layer depth changes are largely confined to the boundaries, an area within 7° of the equator, and the eastern side. Some of the slowly propagating Rossby modes generated at $t = 0$ already have moved away from the eastern boundary. This is clear from the extra-equatorial flow pattern. Behind (i.e., to the east of) this region of equatorward flow in the lower layer (Fig. 6b) there is a region of poleward flow due to the reflection of the Kelvin modes which arrived at the eastern side at day 20. The lower layer flow is eastward at all longitudes on the equator. This transient "undercurrent" is weak (u^2 <.10 m sec^{-1}) and narrow, with a frictionally determined half-width of less than 50 km. The direct cause of this eastward flow at depth is the pressure gradient force (Charney, 1960).

By 397 days (Fig. 7) the model ocean is close to a steady state everywhere in the basin with the exception of the northwest and southwest corners. The upper layer is given primarily by a wind-drift-frictional balance [see I, Eq. (4.1)]. There is strong upwelling along the equator with fluid being returned to the lower layer in downwelling regions at the northern and southern boundaries, the western end of the equator, as well as the latitudes near the equator ($\cong \pm 1°$) where v^s decreases rapidly. There are no exceptionally fast boundary currents. The "undercurrent" maximum velocity is only .2 m sec^{-1} and its half-width is only .5°, numbers determined by the vertical eddy viscosity.

In general, the lower layer flow has an equal and opposite mass flux so that the vertically integrated transport is zero. However, near the equator there is a region of net transport evident in Fig. 7b. This was predicted in I: this net transport is induced by the friction at the bottom of the lower active layer; without this bottom friction the transport would be zero everywhere. As predicted, this circulation occurs in an equatorial boundary layer which thickens from east to west, with predominately zonal transports increasing toward the west. Transport at the equator is in the direction of the wind, while an important signature of the observed undercurrent is that the vertically integrated transport at the equator be large and eastward. Nonlinear dynamics must be included to obtain a realistic undercurrent.

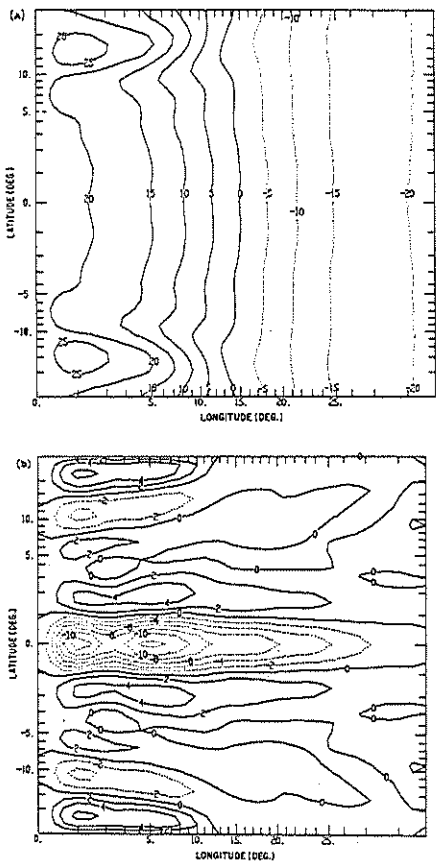

Figure 7. Linear response to an easterly wind at day 397. (a) h. Contour interval is 5 m. (b) Zonal transport u. Contour interval is 2 m^2 sec^{-1}.

4. Nonlinear response to a uniform easterly wind

In this section we consider the nonlinear response to a uniform east wind. Except for the nonlinearity the governing parameters are identical to those in the previous section. Among the simple wind stress patterns this is the one most closely related to the undercurrent in the Atlantic and Pacific Oceans. We first give a narrative description of the numerical experiment and then consider the governing dynamics.

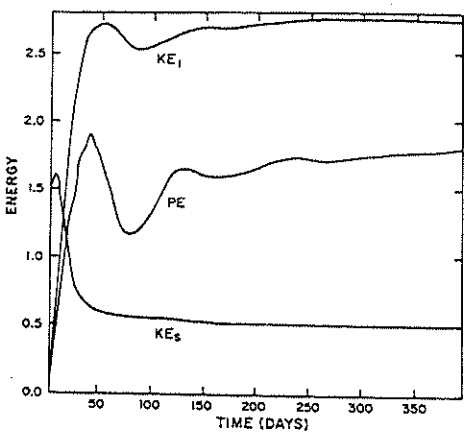

Figure 8. Evolution of energies in the equatorial region for the nonlinear response to an easterly wind. Like Fig. 3. Initial time is 5 days.

a. Evolution of the flow. The energies (Fig. 8) exhibit striking differences from those for the linear response to the same forcing (Fig. 3). The inclusion of vertical momentum advections results in much greater kinetic energy in the lower layer while the surface layer kinetic energy is smaller in the nonlinear case. The upper layer kinetic energy reaches a peak after 9 days, after which it falls off rapidly until day 40.

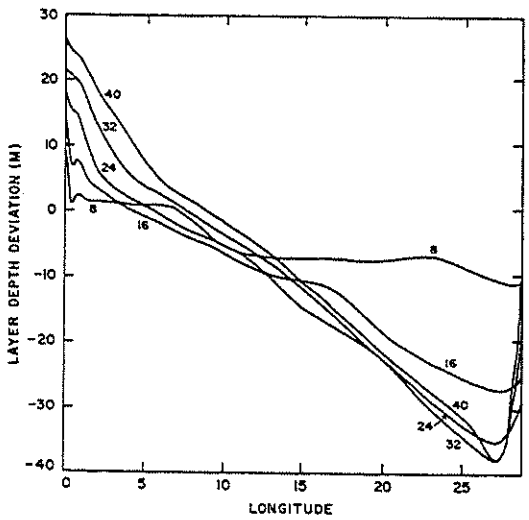

Figure 9. Sections of h along the equator at 8 day intervals in the nonlinear response to an easterly wind. Like Fig. 4.

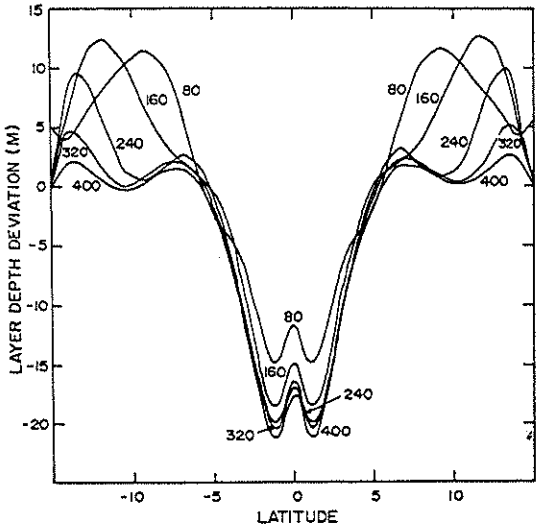

Figure 10. Sections of h along the central longitude $x = 14.3°$ at 80 day intervals in the nonlinear response to an easterly wind. Like Fig. 5.

During this initial 40 day period the potential energy and lower layer kinetic energy both rise to a peak. The loss of surface layer energy to the lower active layer via vertical advections is not fully compensated by the transfer of energy from the winds to the ocean. There is a strong contrast between the linear and nonlinear responses in the oscillations in the energy curves. (These oscillations may be used as an index of the tendency to "overshoot" the final adjusted state as the flow evolves.) The addition of nonlinear effects has damped the tendency to oscillate about a final steady state. Furthermore, the nonlinear steady state is one with potential energy close to the maximum value the system attains in the course of its evolution, while the linear steady state is close to a minimum.

We can see how these differences arise by considering sections of layer depth h at the equator. Figures 9 and 4 show h at the equator for the first 40 days in the nonlinear and linear cases respectively. Throughout this period there is little difference in the two cases, except at the eastern side. Recall that over the first 20 days, the linear response built up a steeper height gradient than was needed to balance the wind stress. After that the reflection of the first Kelvin mode to arrive from the western side caused the layer depth to decrease. The nonlinear case is similar for the first 20 days, but the eastern boundary response to the first signals arriving from the western side is quite different. The slope of h remains steep throughout the basin with a strong boundary layer forming at the eastern wall. Within this narrow (1.5° wide) layer the transports impinging on the eastern wall are turned to the north and south.

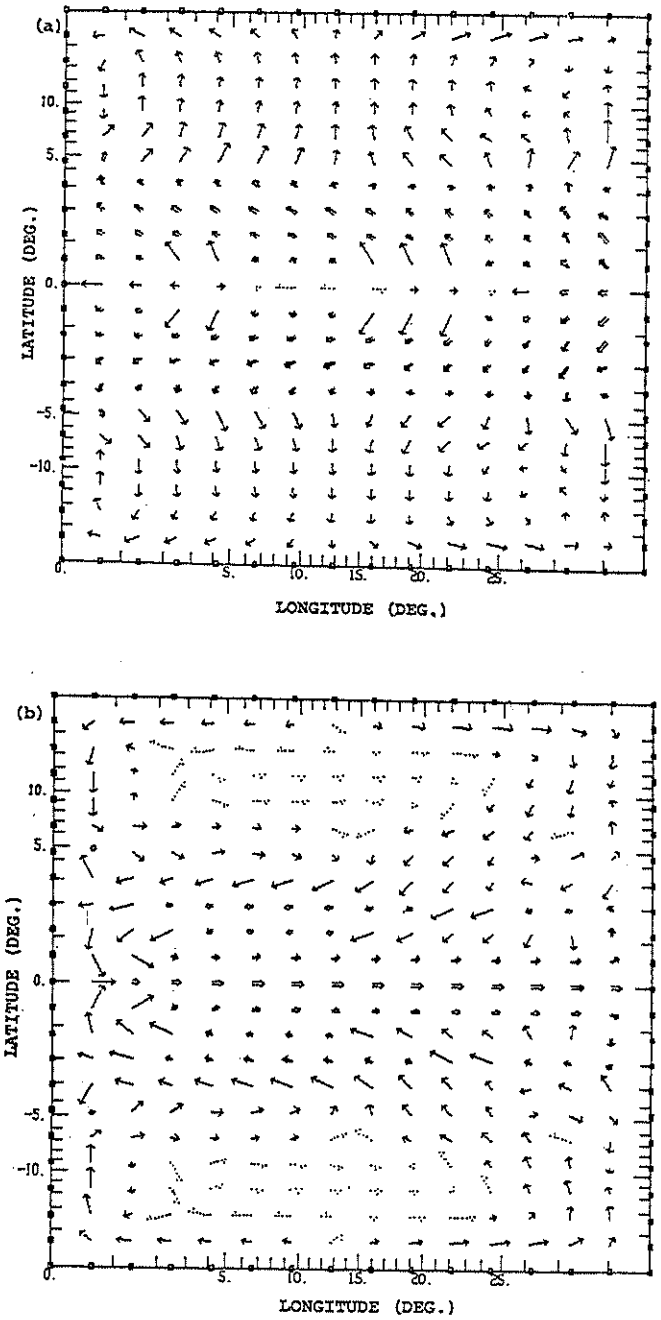

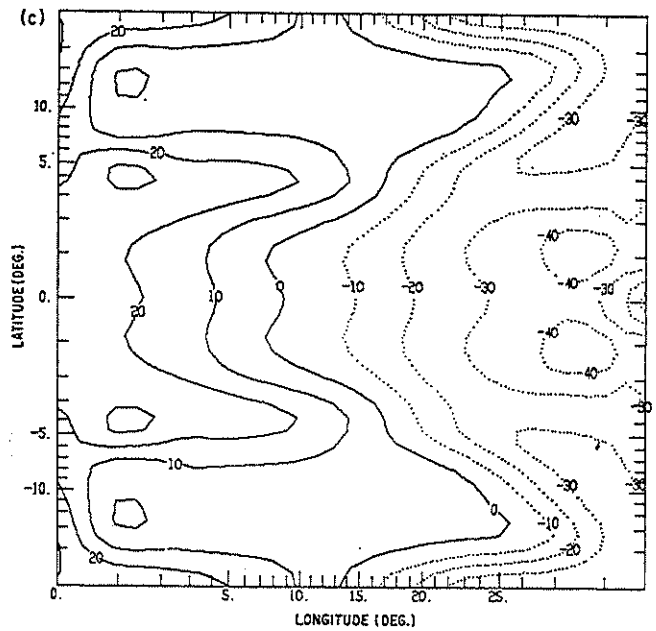

Figure 11. Nonlinear response to an easterly wind at day 40. Like Fig. 6. (a) u' (b) u^2 (c) h. Contour interval is 10 m.

We might say that the nonlinear dynamics respond to the incoming currents at the equator by forming an inertial boundary layer whereas the linear response is a reflection. The Rossby modes which comprise the reflection of the Kelvin mode in the linear theory all propagate too slowly to the west to escape from the boundary in the face of the fast eastward current that exists at the equator. Therefore, they are trapped at the eastern wall on the equator and a boundary layer forms. The layer depth profile evident at day 40 persists thereafter, with its minimum becoming more pronounced with time. After 160 days it varies little.

By 16 days the nonlinear transports along the equator are everywhere eastward, a feature which persists thereafter. The (frictional) linear transports eventually became westward everywhere, but they took on the order of 200 days to do so at all longitudes. After one month has elapsed the transports in the nonlinear case are almost an order of magnitude larger. As discussed below, the differences may be explained in terms of the inclusion of relative vorticity in the nonlinear vorticity balance.

Thus far we have considered the solution at the equator only. Figure 10 shows a meridional section of h at the center of the basin. The greatest difference from the corresponding linear section (Fig. 5) is the deep trough within 5.6° of the equator.

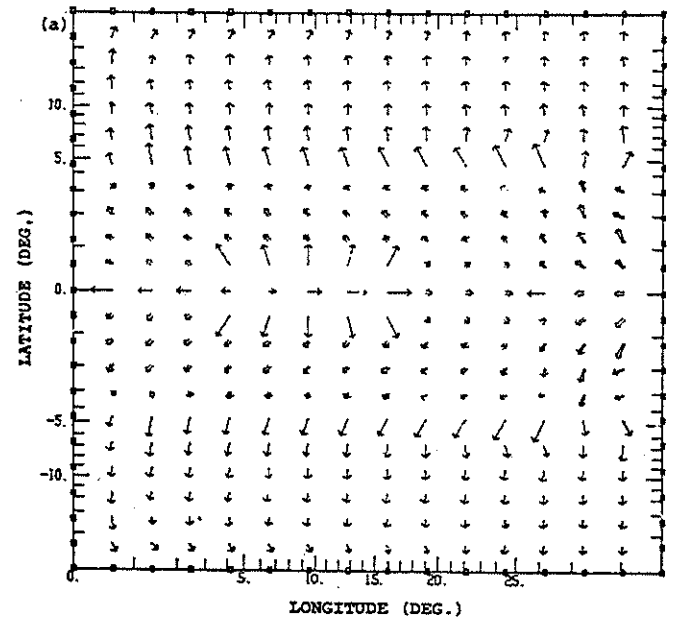

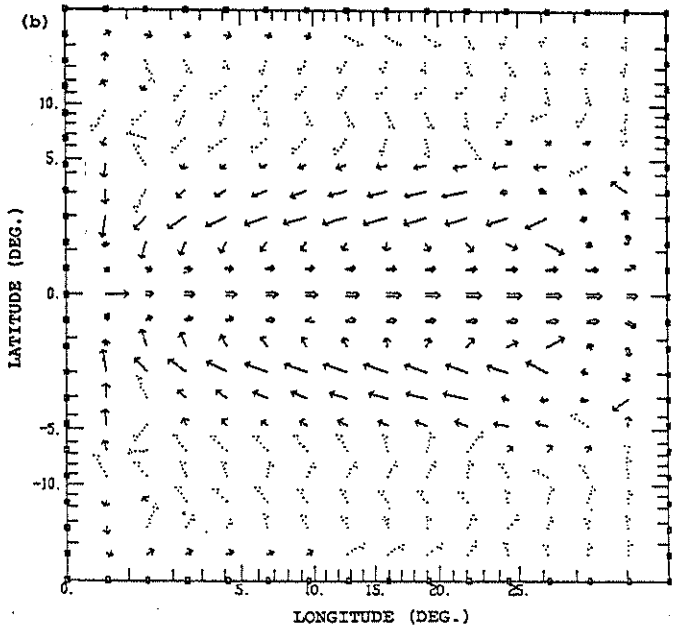

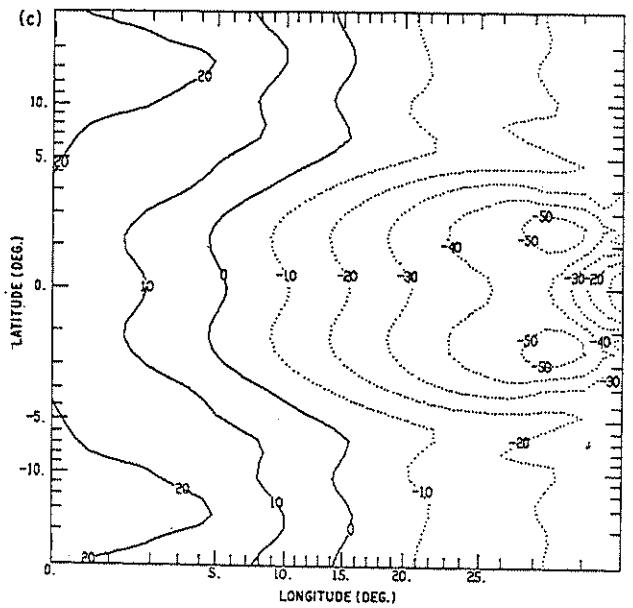

Figure 12. Nonlinear response to an easterly wind at day 398. Like Fig. 7. (a) u' (b) u^2 (c) h. Contour interval is 10 m.

This trough is symmetric about the equator; h slopes downward from 5.6°N to 1.2°N to geostrophically balance the westward current in the lower layer at those latitudes. From 1.2° to 0° it slopes upward to geostrophically balance the undercurrent. By 160 days this trough is close to its final shape. This time scale for adjustment agrees with that given by the energies and the vertically integrated transport at the equator. Within this equatorial region there is some tendency for the adjustment to occur soonest at the eastern side, particularly poleward of about 3°. Poleward of 5.6° the adjustment clearly proceeds from east to west and is more rapid the nearer to the equator one is. The time scales for this extra-equatorial process are comparable to those for the linear case, although h shows some influence from nonlinear effects at all latitudes.

Figure 11 shows the flow at 40 days. The surface layer currents near the equator are more zonally oriented than in the linear case (Fig. 6). This is a result of the fact that parcels tend to turn anticyclonically as they move poleward from the equator and lose relative vorticity to compensate the gain in planetary vorticity. The effects of upwelling, vertical friction and the pressure gradient have reduced the surface layer zonal velocity to near zero at the equator, except at the sidewall boundaries. Vertical advection of eastward momentum from the lower active layer is the most important factor in bringing about this weak surface flow. The maximum undercur-

rent velocity is now above .8 m sec^{-1} and occurs near the eastern boundary. At 14 days this maximum was only .3 m sec^{-1}; by 80 days it is over 1 m sec^{-1}, very close to its final steady value.

At 398 days (Fig. 12) the steady state solution is closely approximated everywhere in the basin with the exception of the northwest and southwest corners. The equatorial region resembles day 40. Poleward of 5° the flow is essentially linear: the surface layer flow is the wind drift solution given by the linear theory while the subsurface flow combines with this to give approximately zero vertically integrated transport. Many of the prominent features near the equator in the interior are in good agreement with the y-z plane calculation of Charney and Spiegel (1971). (See their Figs. 1b and 2b.) Specifically, in both our calculation and theirs the halfwidth of the undercurrent is about 1° and the mean undercurrent velocity is about .80 m sec^{-1}. Both have eastward flow at the surface; as noted above this is primarily due to the strong upwelling at the equator. Eastward flow at the surface with easterly winds has been observed in the Pacific by Taft *et al.* (1974). Both calculations show the strongest westward subsurface flow (on the order of 10 cm sec^{-1}) between 2° and 3°.

b. Basic dynamics. The principal features of the flow may be explained qualitatively by considering the vorticity balance, as in Fofonoff and Montgomery (1955). (Also see Charney, 1960, and Charney and Spiegel, 1971). The easterly wind produces a poleward Ekman drift in the surface layers. This requires upwelling at the equator and therefore an equatorward flow at depth. Parcels moving toward the equator lose planetary vorticity. If we assume that total vorticity is approximately conserved these parcels must acquire relative vorticity as they approach the equator resulting in an eastward flow there. A simple calculation shows that a parcel originating at a latitude y_0 with approximately zero relative vorticity and zero zonal velocity has an eastward velocity of approximately $\beta y_0^2/2$ at the equator. For undercurrent velocities of .75 to 1.00 m sec^{-1} y_0 is between 2.5° and 3°; this is consistent with our calculation. A similar line of reasoning may be used to determine the position of the westward currents. Fluid parcels in the undercurrent that reach the eastern side are turned poleward in narrow boundary currents. As they travel away from the equator they gain planetary vorticity. In order to approximately conserve their vorticity they must lose relative vorticity so that their poleward velocity must decrease (since in these currents relative vorticity $\zeta \approx v_x$). In particular, if the vorticity of such a parcel is βy_0 it cannot progress poleward beyond the latitude of y_0. We conclude that this will be the latitude of the currents required to complete fluid circuits that include the undercurrent.

This vorticity argument may obscure the nonlocalness of the dynamics because it makes no explicit mention of the essential role played by the zonal pressure gradient. In the absence of a zonal pressure gradient, angular momentum conservation would

argue the parcels of fluid arrive at the equator with westward velocity. In fact, the pressure forces accelerate the lower layer flow eastward. Further, for the subsurface flow to have an equatorward component requires a zonal pressure gradient for geostrophic balance. Without this gradient the lower layer fluid demanded by the intense upwelling at the equator is supplied by having the thermocline rise with time. This is what happens in the early stages of the experiment at longitudes where neither the eastward traveling Kelvin nor westward traveling Rossby modes have yet arrived to set up the pressure gradient. Such behavior should be expected from the linear analysis: Eq. (3.1) clearly shows that the layer depth will decrease with time as long as there is no zonal variation. It is only after the initial boundary responses (Kelvin and Rossby) meet that the undercurrent becomes established.

The vorticity arguments presented above may be extended to estimate the latitude y_0 where the undercurrent water originates. Poleward of y_0 the advection of planetary vorticity in the lower layer is balanced by the vortex stretching term fw; y_0 is the point where nonlinear terms enter the vorticity balance. In I Sec. 2 we established that the linear dynamics of the Ekman layer break down at a latitude y_e when inertial terms become important in the Ekman layer. The latitude y_0 must be the same order as y_e since the layers are coupled by vertical motions. These considerations allow us to find a frictional-inertial scaling for Eqs. (1.1), valid when the Ekman layer Rossby number $\epsilon_E \equiv \epsilon\gamma^{-1/2}$ satisfies $\epsilon_E^{-1/5}\gamma^{1/2} \ll 1$. [See (1.2) for the definitions of ϵ and γ. For the parameter values in Table 1, $\epsilon_E \approx .2$ and $\gamma \approx 10^{-2}$.] The arguments of I give the following rescalings in Eqs. (1.1):

$$y = \epsilon_E^{2/5}\, y'; \quad \alpha = \epsilon_E^{-1/5}\,\gamma^{1/2}\,\alpha'; \quad \gamma_I = \epsilon^{1/5}\,\gamma^{1/2}/\alpha' . \tag{4.1}$$

We assume that the scale in the x direction is long enough so that zonal variations may be neglected except in the pressure gradient term. (It is this term which drives the undercurrent.) It then follows from (4.1) that the remaining variables may be written (cf., Philander, 1971, p. 239):

$$(u^s, v^s, u^1) = \epsilon_E^{-1/5}\,\gamma^{-1/2}\,(u^{s\prime}, v^{s\prime} u^{1\prime}) ; \tag{4.2}$$

$$v^1 = \epsilon_E^{-2/5}\, v^{1\prime}; \quad w_e = \epsilon_E^{-4/5}\, w'_e ;$$

$$h = \int^x \tau^{(x)}\,(y{=}0)\,dx + \gamma^{-1/2}\,\epsilon_E^{3/5}\,\rho$$

We now have scalings in terms of the governing parameters for all variables in the equatorial region. In dimensional terms the meridional scale for the equatorial circulation is 1.5°. The scale for the surface velocities and the subsurface zonal velocity is $[\tau_0^4/4\beta\nu_v^2]^{1/5}$; this is about .5 m sec^{-1}. (We have again taken $K \approx 2\nu_v/\bar{H}$).

Dropping primes and taking $\alpha' = 1$ for simplicity the steady state version of (1.1) is

$$v^s u_y^s + \tfrac{1}{2}\, w_e\,(u^s - u^1) - y\, v^s - \tau^{(x)} = 0 , \tag{4.3a}$$

$$v^s v_y^s + \tfrac{1}{2} w_e v^s + y u^s + \rho_y = 0\,, \tag{4.3b}$$

$$v^1 u_y^1 + \tfrac{1}{2} w_e (u^s - u^1) - y v^1 + \tau^{(x)} = 0\,, \tag{4.3c}$$

$$y u^1 + \rho_y = 0\,, \tag{4.3d}$$

$$v_y^s + v_y^1 = 0\,, \tag{4.3e}$$

$$w_e - v_y^s = 0\,. \tag{4.3f}$$

The meridional sections of the layer depth that we calculate (Fig. 10) agree qualitatively with the bowing of isotherms which is usually observed beneath the undercurrent (e.g., Knauss, 1966). Eq. (4.3d) requires that the pressure gradient be in geostrophic balance with the lower layer zonal velocity. This accounts for the meridional profile of the pressure gradient. For example, at the center of the basin at .3N the terms fu and $g'h_y$ balance to within 10%. At 3N the balance is within 15%.

c. Longitudinal variations. By considering Eqs. (4.3) at the equator we may easily see that terms neglected in those equations must enter the momentum balance. Since symmetry dictates that $v^1 = v^s = 0$, (4.3a) says that the vertical advection term balances the wind stress while (4.3c) demands that the same term balance the zonal pressure gradient ($-\tau^{(x)}$). Since the surface stress and the pressure gradient are of opposite sign this is not possible. This argument is not an artifact of our two-level model: it applies to a continuous ocean from the surface down to the undercurrent velocity maximum, a region where w is positive and u_z negative.

It is Eq. (4.3c) that must break down. Two types of terms have been neglected there: those due to vertical friction and those that arise from longitudinal variations. Vertical viscosity is already essential in (4.3) because of its role in the surface frictional Ekman layer; what is at issue here is its direct role in limiting the growth of zonal momentum in the undercurrent. Vertical friction terms enter (4.3) at $0\ (\epsilon_B^{-1/5}\gamma^{1/2})$ — about an order of magnitude smaller than the retained terms for the parameter values we use. Charney and Spiegel's (1971) model fixes the value of the zonal pressure gradient and excludes other zonal variations *a priori* so that vertical viscous forces offer the only possible balance in a steady state undercurrent. In this context we note that their calculations failed to converge when the eddy viscosity was reduced to 13 cm^2s^{-1}, leaving only the acceleration term to balance the pressure force.

In our model longitudinal variations are permitted and the zonal pressure gradient is free to seek its own value. The usual argument for neglecting longitudinal variations (e.g. Charney and Spiegel, 1971) is that the inertially determined cross stream scale $\epsilon_B^{2/5}$ is so much smaller than the downstream scale L_x. However, it is inappropriate to simply compare length scales because the subsurface velocity components have different scales.

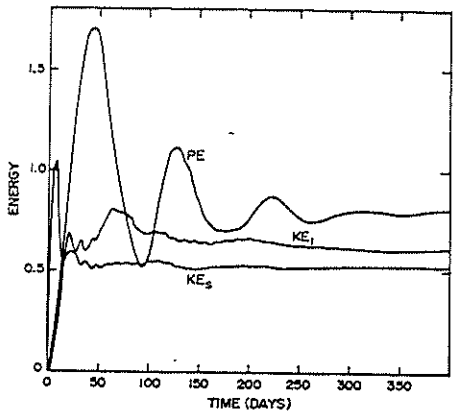

Figure 13. Evolution of energies in the equatorial region for the nonlinear response to a westerly wind. Like Fig. 3.

In (4.3c) terms involving zonal variation (i.e., $u^1 u_x^1$ and p_x) will enter before the vertical viscous terms as long as the zonal length scale L_x is less than $\gamma^{-1}\epsilon_B^{2/5} = 10^4$ km (for our parameter values). Hence these terms are more important than the frictional ones. The most stringent condition for neglecting zonal variations altogether in (4.3) is that $L_x >> \gamma^{-1/2}\epsilon_B = 1300$ km. This is large enough so that we should expect zonal variations to be dynamically significant, an expectation borne out by our numerical experiment. [It is the downstream acceleration $u^1 u_x^1$ that balances the pressure gradient in (4.3c).]

5. Nonlinear response to a uniform westerly wind

We now consider the nonlinear response to a uniform westerly wind stress. The only parameter changed from the previous section is the wind direction. The responses in the two *nonlinear* cases are quite different because the beta effect causes east-west asymmetries in the ocean dynamics. On the other hand, the *linear* responses are very much the same. The east wind response (Sec. 3) becomes the west wind response simply by changing the sign of all variables (h into $-h$, u^s into $-u^s$, etc.); the *pattern* of the response is unaltered.

The energy plot for this case (Fig. 13) resembles that for the linear east wind (Fig. 3) more than the nonlinear one (Fig. 8). The potential energy curve for the present case is almost identical to that for the linear case: the amplitudes are approximately the same and the oscillations have the same periods. In Sec. 3 these oscillations were shown to result from the reflections of Rossby and Kelvin waves at the meridional boundaries and the same explanation applies here. Unlike the east wind nonlinear case, the undercurrent does not become strong enough to significantly

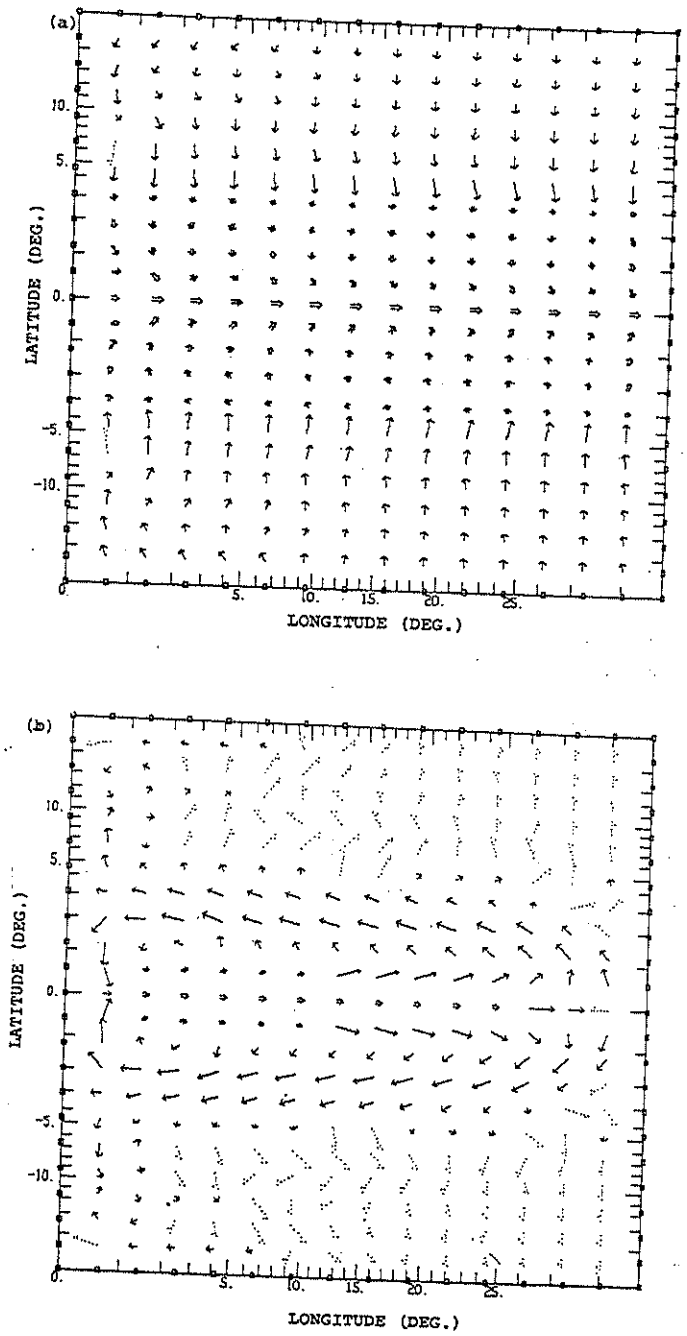

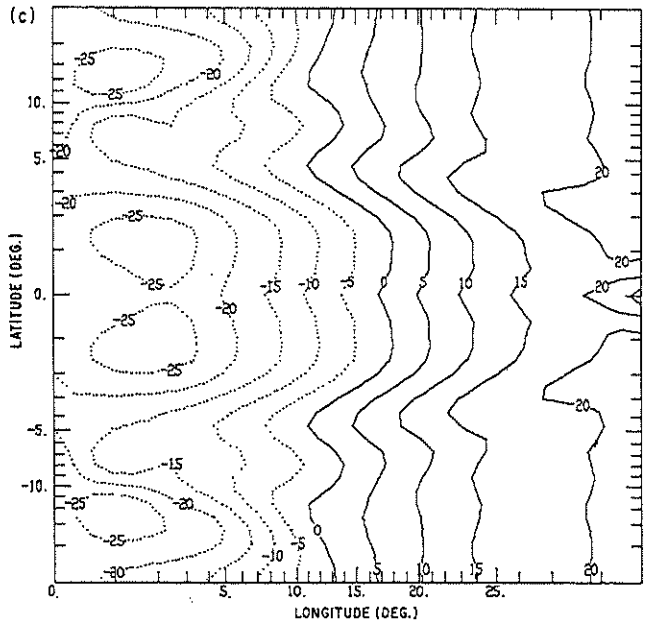

Figure 14. Nonlinear response to a westerly wind at day 398. Like Fig. 7 (a) u' (b) u^1 (c) h. Contour interval is 5 m.

interefere with the Rossby wave reflections at the eastern side. The layer depth evolves much as it did in the linear case. In contrast to the east wind nonlinear case (and like the linear one) the final zonal pressure gradient very nearly balances the wind stress. The inclusion of vertical advection of momentum makes the distribution of kinetic energy different from the linear case, with the surface layer being less, and the lower layer more, energetic. In this it is like the other nonlinear case but the lower layer kinetic energy is much smaller here.

At the equator the vertically integrated zonal transport $\bar{u}$ becomes close to its final interior value within 8 days though there is some oscillation about this final value (of about 75 m^2 sec^{-1}) until about day 160. The nonlinear east wind case takes about 24 days to reach a value of 75 m^2 sec^{-1} and about 80 days to approximate its final value of 140 m^2 sec^{-1}. In both the east and west wind cases the steady state requires westward currents off the equator to return the water that has travelled to the eastern side at the equator. In the west wind case these lower layer currents, centered at 2S and 2N, take longer to become established. They are absent before day 40 and take 80 days to approach their final value, so the early evolution supplies the net eastward transport of water needed to set up a zonal pressure gradient opposite to the wind. When the wind is from the east the westward flowing currents are set up before the eastward flowing undercurrent.

By day 398 (Fig. 14) a steady state is closely approximated everywhere in the model basin with the exception of the northwest and southwest corners. The surface layer currents are very much as they were at day 8 with the extra-equatorial wind drift currents turning within a degree of the equator to form an eastward jet. In the lower layer there is a slower equatorial eastward jet with a half width of 1°. The water transported eastward at the equator in both layers is returned to the west in lower layer currents extending from about 1° to about 4° on both sides of the equator. There is very strong downwelling at the eastern end of the equator in order to transport the upper layer water into the lower layer so that it may return to the west.

The currents at the equator are established within a week. The wind-drift balance yields equatorward flow in both hemispheres. As argued in the last section, approximate conservation of vorticity results in parcels having eastward momentum as they approach the equator. There they are further accelerated by the direct action of the wind stress. Convergence at the equator demands downwelling, with a consequent advection of eastward momentum into the lower layer resulting in subsurface eastward flow. This process is set up on the frictional timescale, unlike the east wind response. The vorticity argument requires equatorward flow: for the west wind this results from frictional-Coriolis (i.e., Ekman) effects while the east wind response required that the large scale zonal pressure gradient be set up. The dynamics in the west wind case are local as well as rapid. A patch of westerlies at the equator will quickly produce subsurface eastward flow while a similar patch of easterlies will not. In the initial stages of the west wind experiment the downwelling resulting from convergence at the equator depresses the thermocline. Later, when the zonal pressure gradient is set up, subsurface poleward flow removes the fluid brought in at the surface and the layer stops deepening. This is the steady state circulation pattern.

6. Linear response to a uniform southerly wind

The linear response to a uniform south wind has zonal velocities and layer depth antisymmetric and meridional velocities symmetric about the equator. The analysis presented in I and CSII describe this response rather thoroughly. While little is added by the numerical solution, a review of this case is a useful prelude to nonlinear results of the next section.

The surface layer velocity $\mathbf{u}^s$ is given by the frictional velocity $\tilde{\mathbf{u}}$: a strong northward current in a frictional boundary layer centered on the equator gives way to eastward and westward wind drift currents in the northern and southern hemispheres, respectively (Fig. 15a). This flow sets up on the frictional timescale and is well established within 10 days after the wind stress is switched on. In the absence of bottom friction the steady solution has zero transport with the sea surface tilted up to the north to balance the wind: $\tilde{\mathbf{u}} = 0$, $h = y\tau^{(y)}$ (with the scaling of Sec. 1). The analysis of CSII shows that this state is approached monotonically with the adjust-

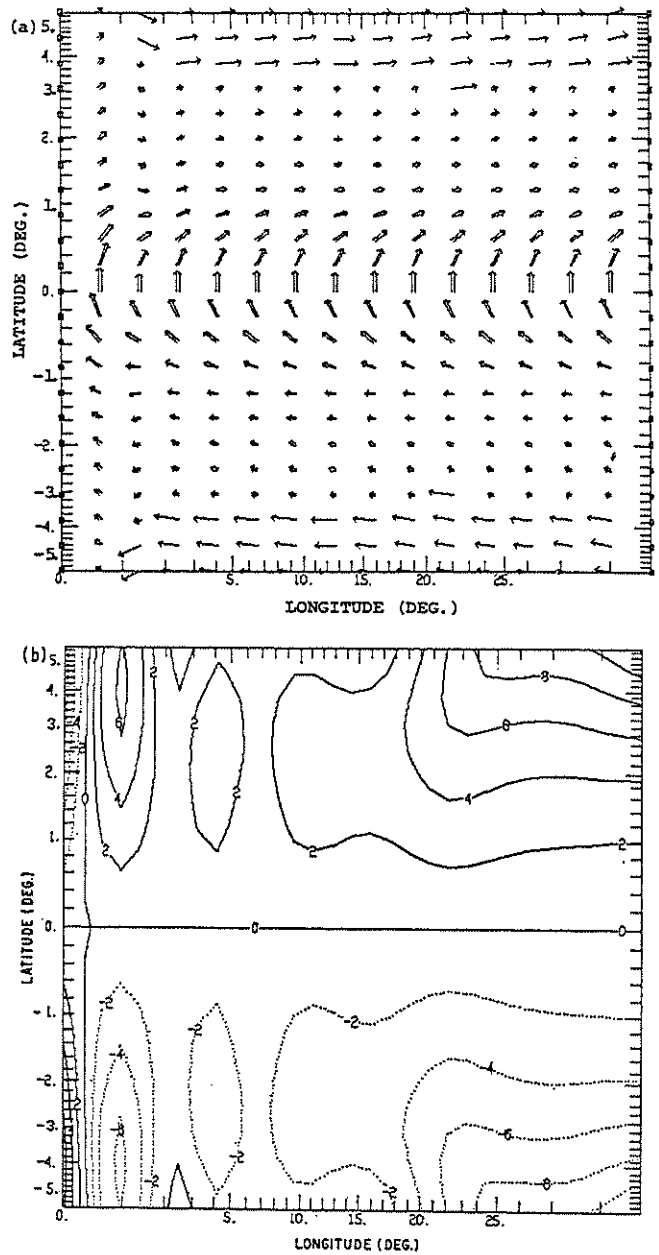

Figure 15. Linear response to a southerly wind at day 40. Like Fig. 6 but only the equatorial region (5.6S to 5.6N) is shown. (a) $\mathbf{u}^s$ (b) h. Contour interval is 2 m.

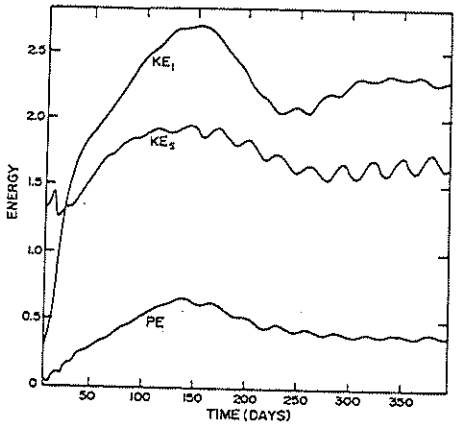

Figure 16. Evolution of energies in equatorial region for the nonlinear response to a southerly wind. Like Fig. 3. Initial time is 5 days.

ment proceeding from east to west and from the equator poleward. No Kelvin waves are excited so the adjustment is effected entirely by long wave Rossby modes. Because of the absence of Kelvin waves there is nothing like the oscillation shown by the linear response to an east wind. Since bottom friction is present the steady state has an equatorial boundary layer with nonzero transports. The characteristics of this layer are in detailed agreement with the analytic results of I. By far the largest part of the ocean's energy in the equatorial region is in the surface layer motions. As in the previous linear case there is little kinetic energy in the lower layer. Since $h \lesssim y\tau^{(y)}$ for all time there is little potential energy near the equator where y is small.

Figure 15b shows the layer depth at 40 days. The northward tilt is clearly evident at the eastern side. The lower layer currents are in geostrophic balance (except for the area along the equator where the pressure force is frictionally balanced by southward flow). At the western side h has strong gradients to balance the meridional boundary currents evident in both layers. The southward current east of the boundary current is required by conservation of potential vorticity. Mathematically, it results from the Bessel function behavior of the western boundary layer solution (cf. CSII, Fig. 2).

7. Nonlinear response to a uniform southerly wind

An overview of the spin up process is given by Figure 16, which depicts the energy in the equatorial region. As in the linear case, the surface layer kinetic energy quickly (order 8 days) rises to within e^{-1} of its final value as the wind stress transfers energy to the ocean. Thereafter, the increase in surface energy and potential energy continue until about day 150. The lower layer kinetic energy becomes

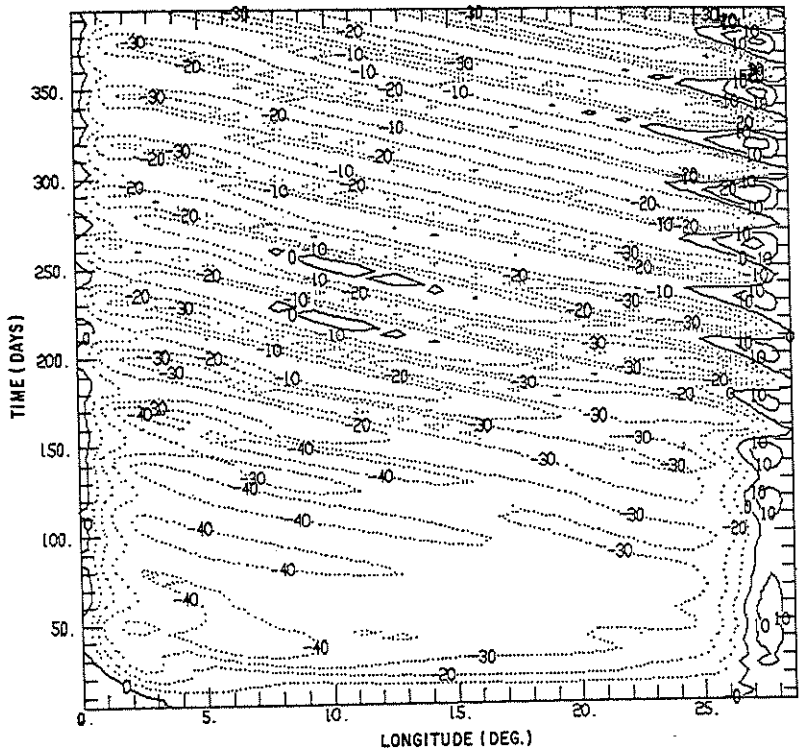

Figure 17. Contours of lower layer zonal velocity, u^2, along the equator as a function of time for the nonlinear response to a southerly wind. Contour interval is 10 cm sec^{-1}. Note the regular westward phase progression.

almost an order of magnitude larger than in the linear case indicating the importance of vertical advection as a mechanism for transferring momentum to the lower layer.

Beginning at about day 100 an oscillation with a period of 29 days may be observed in the surface kinetic energy. At about 150 days, an oscillation in the potential energy sets in approximately in phase with this. The lower layer kinetic energy starts to decrease, eventually leveling off to oscillate about a steady value, the oscillations being out of phase with those in the other quantities. This suggests an instability which draws its energy primarily from the kinetic energy of the flow. Figure 17 shows a plot of phase lines of the lower layer zonal velocity at the equator—the abscissa is distance along the equator, the ordinate is time. Beginning near the western side at about day 100 and appearing later at the eastern side, a very regular progression of phase from east to west may be observed. (Similar plots of the other variables give essentially the same picture.) These waves have a period of 29 days and a phase speed of 32.5 km/day, giving a wavelength of 950 km.

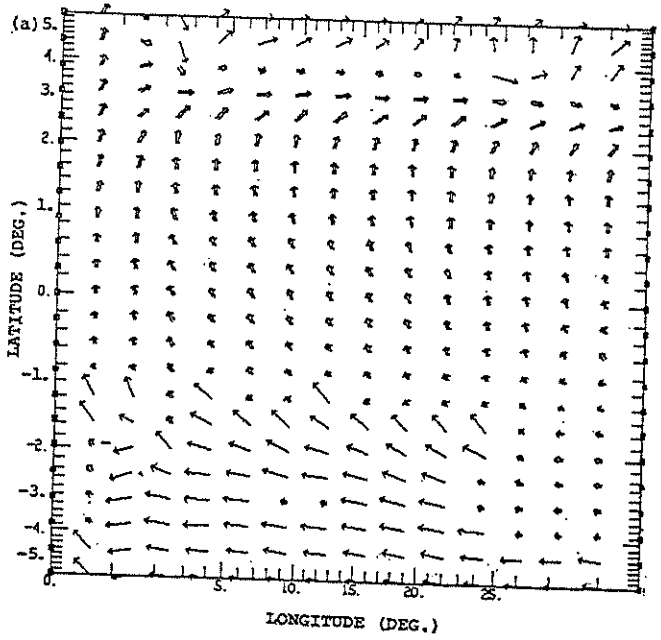

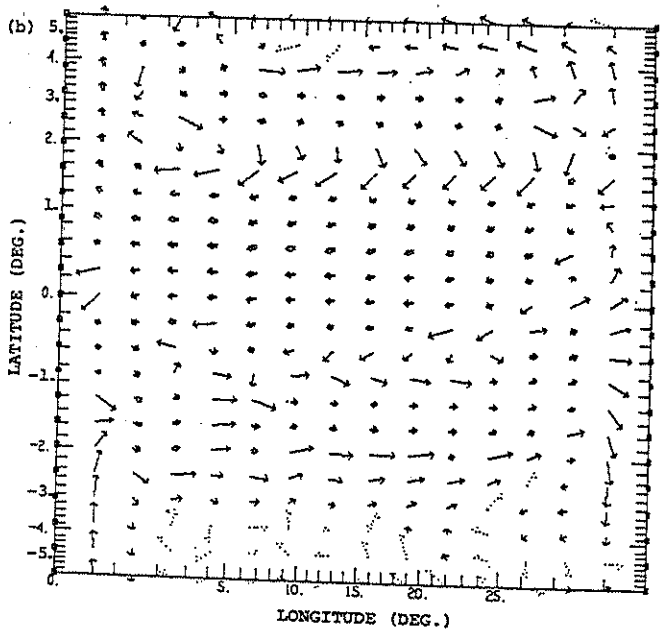

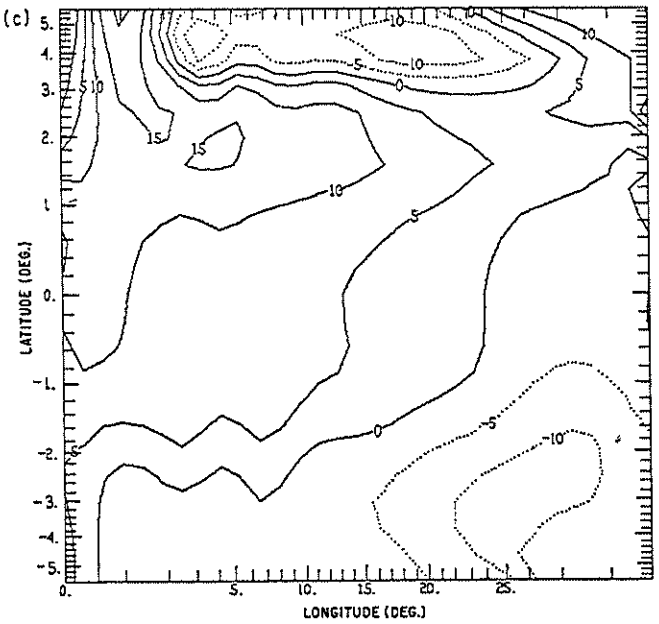

Figure 18. Nonlinear response to a southerly wind at day 40. Like Fig. 15. (a) u' (b) u^2 (c) h. Contour interval is 5 m.

a. Evolution of the flow. In the early stages many of the features of the flow pattern can be understood by considering the kinematic effects of the vertical and meridional advections on the linear response. At 8 days the circulation pattern in both layers is similar to the linear response at the same time, but some departures from the linear symmetries are already apparent. In the surface layer the maximum meridional velocity occurs at approximately 1N, rather than on the equator as in the linear response. This difference is due to the self-advection of northward momentum by the surface currents near the equator. A similar advective effect is observable in the zonal component of the surface current. Westward momentum has been advected northward across the equator so that the surface flow is westward to 1.2N. The eastward momentum in the surface layer north of the equator has also been advected northward—but not beyond 3N, where the meridional velocity goes to zero. The effect is to compress the eastward flow into a narrower, more intense jet. The eastward flow at 2.5N is at speeds of .9 ms^{-1}, compared to the linear maximum of .6 ms^{-1} at 1.2N. The trend is thus toward the development of an eastward jet at 2.5N with a broader, slower westward flow at the equator. At this time, vertical velocities are negligible everywhere in the interior and currents in the lower layer are small.

The results of this development are evident at day 40, Figure 18 (cf. the linear case Fig. 15). The eastward jet is now centered at 3N. There is a considerable horizontal convergence into the jet, resulting in substantial downwelling; elsewhere in the interior the vertical velocity is negligible. This downwelling advects eastward momentum into the lower layer so that the flow there is also eastward (Fig. 18b). The result is a large vertically integrated transport to the east—a factor of 5 larger than in the linear case.

b. The x, t independent flow. The features of the flow evident at day 40 were substantially established within 16 days. The pattern persists with little qualitative change beyond day 100. We note that the interior flow is approximately steady and independent of longitude. [The primary exception to this is the layer depth (Fig. 18c) which shows a more uniform tilt to the north at the eastern side, similar to the linear case. It also shows a suggestion of a wavelength structure at about 4N.] The part of the interior field that is independent of x and t has four dynamically distinct regions:

(i) South of about 2.5S the response is essentially linear, like that discussed in the previous section. The dominant feature is the surface wind drift current to the left of the wind.

(ii) From 2.5S to about 2.5N the surface flow turns from northwestward to northeastward to due east. Vertical velocities are everywhere upward and small [$0(10^{-5}$ m sec$^{-1})$], with most of the upwelling south of the equator. South of 1N u^1 is westward, while north of 1N it is eastward, with a magnitude comparable to u^s near the equator. The meridional component is southward everywhere.

(iii) From 2.5N to 5N there is an eastward zonal jet in both layers: at 3N u^s is as high as 1.2 m sec^{-1}; u^1 is over .4 m sec^{-1}. There is strong surface convergence into the jet with large downwelling at its core ($w = 3 \times 10^{-4}$ m sec^{-1}).

(iv) North of about 5N the model response again becomes wind drift dominated and essentially linear.

This description is in close agreement with the x-independent, steady state calculation of Charney and Spiegel (1971). (See their Figs. 11 and 12.) The only notable disagreements are that their surface velocity in the jet is smaller (less than 1 m sec^{-1}), their downwelling region is broader, and their upwelling region narrower than ours. We now seek a simple model (independent of x and t) to elucidate the physics of this flow.

Regions (i) and (iv) are explicable in terms of linear dynamics. Now consider the surface flow in region (ii). A parcel in the vicinity of the equator will acquire a northward velocity component (frictional forces give it a component in the direction of the wind). As it moves northward, it acquires cyclonic planetary vorticity. Since it (approximately) conserves its total vorticity, it must acquire anti-cyclonic

relative vorticity. The effect is to turn the parcel clockwise toward the east. As long as the parcel moves northward, it is able to acquire energy from the wind stress. At some latitude the parcel's northward momentum is being converted into eastward momentum more rapidly than it is replenished by the wind. Eventually, the parcel will be travelling due east, still carrying the approximately zero total vorticity it had near the equator. To the north of this, the flow is in the wind drift regime where the vorticity of surface parcels is approximately the local planetary vorticity. The transition between the two flow regimes demands a shear layer in which the surface eastward velocity is reduced to the north, thus adding enough positive vorticity to the flow to match it to the planetary vorticity. This accomplished by the downwelling in the jet which transports the eastward momentum downwards.

We may formulate a simple model for the surface flow in region (ii) in order to obtain some quantitative checks to accompany this qualitative description. Neglecting friction the approximate governing equations are

$$\frac{d}{dt} u^s - \beta y v^s = 0 , \tag{7.1}$$

$$\frac{d}{dt} v^s + \tfrac{1}{2} \frac{w}{\eta} + \beta y u^s = \frac{\tau}{\eta} \tag{7.2}$$

Since the flow varies little with t or x, $d/dt \cong v\partial/\partial y$ and $w/\eta \cong v_y{}^s$. Since $v^s u_y{}^s >> v_y{}^s u^s$ the vertical advection term is neglected in (7.1).

An energy equation (which allows for some loss to the lower layer) may be formed from (7.1) and (7.2):

$$\tfrac{1}{2} \frac{d}{dt} \left(u^{s2} + \frac{3}{2} v^{s2} \right) = \frac{\tau v^s}{\eta}$$

By making use of the definition $dy/dt \equiv v$, this may be integrated to yield

$$u^{s2} + \frac{3}{2} v^{s2} = 2 \frac{\tau}{\eta} y + \text{const.}$$

Eq. (7.1), which expresses the conservation of vorticity, integrates to

$$u^s(y) = \tfrac{1}{2} \beta y^2 + u^s(0) .$$

We may now simplify things further by assuming that $u^s = v^s = 0$ at the equator and so obtain

$$u^s \approx \frac{1}{2} \beta y^2; \quad v^{s2} = \frac{4}{3} \frac{\tau}{\eta} y - \frac{\beta^2 y^4}{6} . \tag{7.3}$$

The position of the jet is at latitude y_J where $v^s \approx 0$:

$$y_J \approx 2 \left[\frac{\tau}{\eta \beta^2} \right]^{\frac{1}{3}} \approx 340 \text{ km} \approx 3° .$$

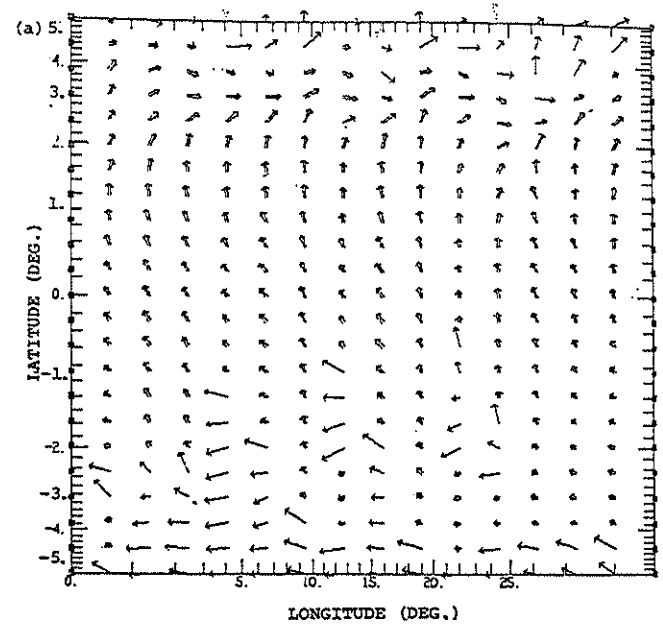

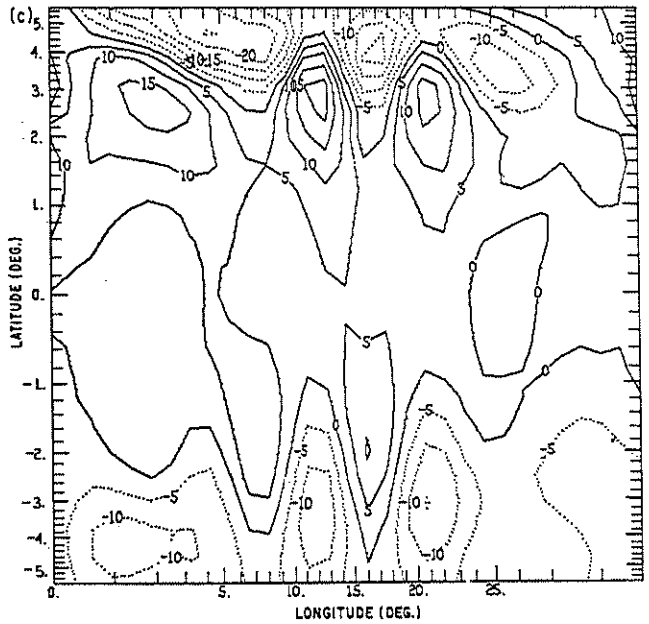

Figure 19. Nonlinear response to a southerly wind at day 398. Like Fig. 18 (a) u' (b) u^2 (c) h.

At this latitude $u_J = \frac{1}{2}\beta y_J^2 \cong 1.2$ m sec^{-1}. These values are in excellent agreement with the numerical calculation. We may also obtain a scale for the other velocity component by considering the latitude y_m where v^s is a maximum. We obtain $y_m \approx 2°$ and $v_m \equiv v_s(y_m) \approx .7$ m sec^{-1}, again in good agreement with the numerical calculation.

Turning now to the jet itself, the requirement that the vorticity of the flow be brought up to the local planetary vorticity in order to match onto the linear regime gives a scale for the width Y of the shear zone:

$$\beta(Y + y_J) \approx u_J/Y \rightarrow Y \approx 1.1°$$

This is the right order but slightly too wide (the model results show $Y = .8°$). One feature of this description which agrees well with the numerical calculation and that of Charney and Spiegel (loc. cit.) is that the zonal velocity of the jet falls off more rapidly to the north than to the south.

The fluid which descends in the jet arrives in the lower layer with considerable eastward momentum and negative relative vorticity. In region (ii) continuity requires that v^1 be southward. Parcels will approximately conserve their total vorticity because vertical exchanges are small and because both f and variations in the layer depth are small (so that the variation of potential vorticity is given by the variation

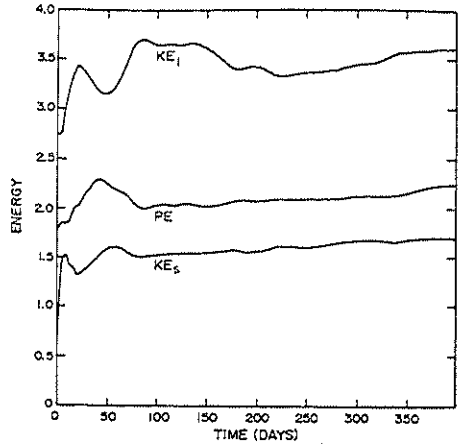

Figure 20. Evolution of energies in the equatorial region for the response to a southeasterly wind. (At $t = 0$ the flow is adjusted to an easterly wind. A southerly component is added so that the wind is then from the southeast.) Like Fig. 3.

of vorticity). As a parcel travels southward, its planetary vorticity decreases so its relative vorticity ζ must become less negative and may even become positive. In our calculation $u_y^1 = 0$ at about .3N. North of this point the flow impinging on the western boundary turns clockwise to the north ($\zeta < 0$), while south of it the flow turns counterclockwise to the south ($\zeta > 0$).

c. Stability. The foregoing analysis has implications for the susceptibility of the flow to shear instability. For nondivergent inviscid flow a necessary (but not sufficient) condition for instability is that the vorticity—$f-u_y$ in our case—have an extremum. Though our situation is more complicated, this simple criterion still serves as a useful guide (see below). This condition is usually not met by geophysical flows because the gradient of planetary vorticity, $\beta-u_{yy}$, is always positive. In region (ii) the flow in each layer is characterized by the conservation of total vorticity, thereby neutralizing the stabilizing effect of beta. The flow is thus marginally unstable; and, in fact, the model calculation does exhibit numerous extrema in the profile of $f-u_y$.

At day 120, a time when the energy curves (Fig. 16) show some evidence of instability, the waviness suggested at day 40 (Fig. 18) at 4N is marked, with a similar wavy pattern developing at 4S as well. At 160 days, when the lower layer kinetic energy reaches a peak, this pattern is no longer confined to the western side, but is present in equal amplitude across the width of the basin. By about day 200, the flow settles into a repeated pattern with wavelike disturbances propagating (in the phase sense) across the basin from east to west (see Fig. 17), though the zonally averaged mean flow is still similar to that at day 40. Figure 19 shows the fields during this final period of the flow's evolution. The variations in the layer depth (Fig.

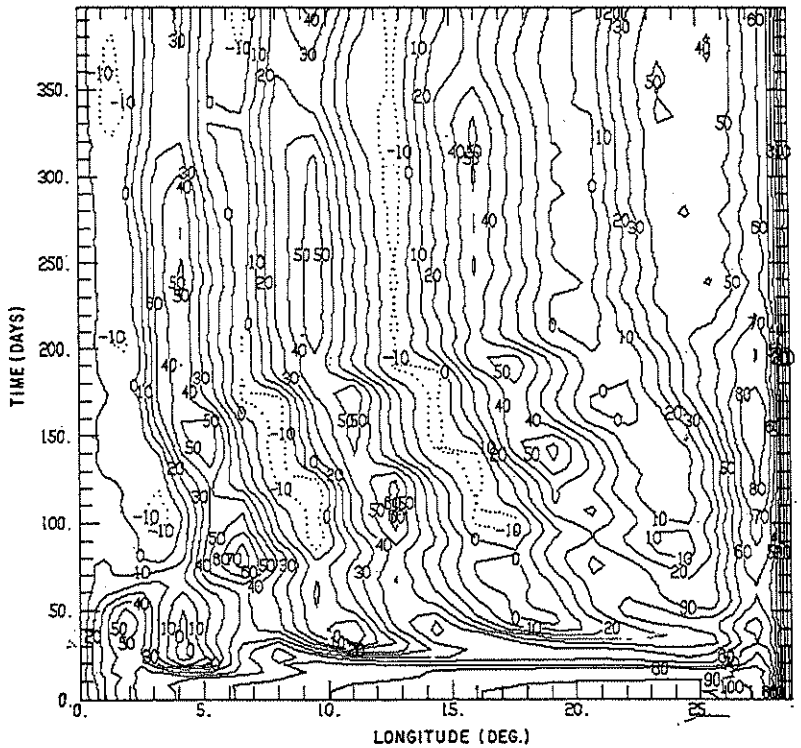

Figure 21. Contours of u^1 along the equator for the nonlinear response to a southeasterly wind. Like Fig. 17.

19c) are dominated by this instability from 7S to 7N, while poleward of these latitudes it exhibits a general south to north tilt similar to the linear case.

It is of interest to compare our results with the results for the stability of equatorial currents given by Philander (1976). On the basis of the vertically averaged zonal velocity we can crudely fit the model currents to a sech^2 profile, viz. $U \cong U_0$ sech^2 $y/L + U_1$, by taking $U_0 \cong -.7$ ms^{-1}, $U_1 = +.4$ ms^{-1} and $L \cong 100 - 200$ km. Then $R_i = gHU_0^{-2} \cong 8$ and $R_0 = U_0\ (\beta L^2)^{-1} \approx -1$ to -4. From Figure 3 of Philander (loc. cit.) the wavelength of the fastest growing wave for these parameter values is approximately $2\pi L$—between 600 and 1,200 km in our case. This is consistent with the model results.

8. Nonlinear response to a uniform southeasterly wind

In this case the initial state is taken to be the steady state response to a uniform easterly wind described in Sec. 4. (To be precise, the initial state is taken as the

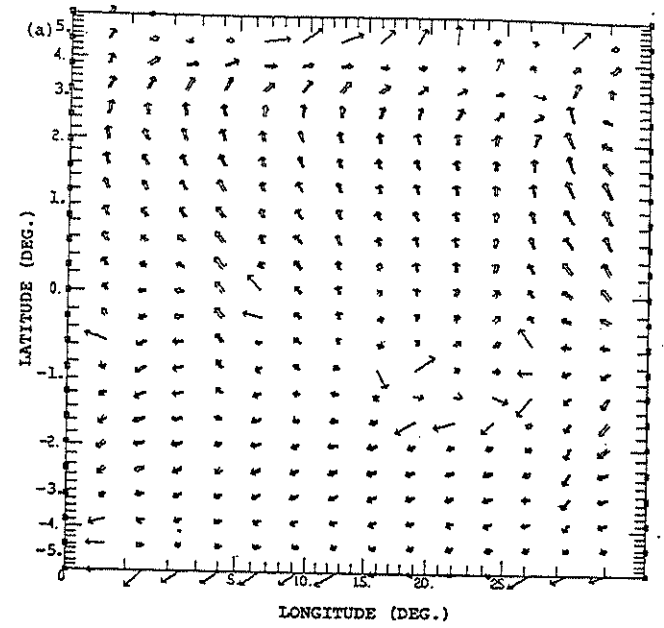

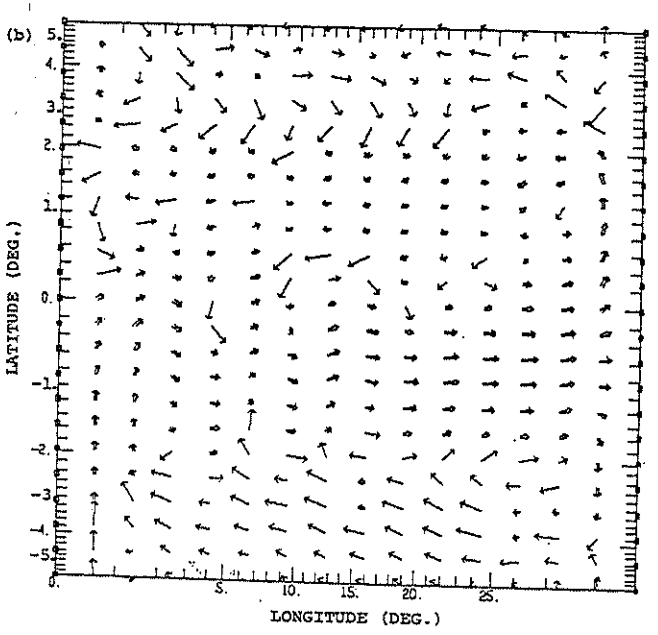

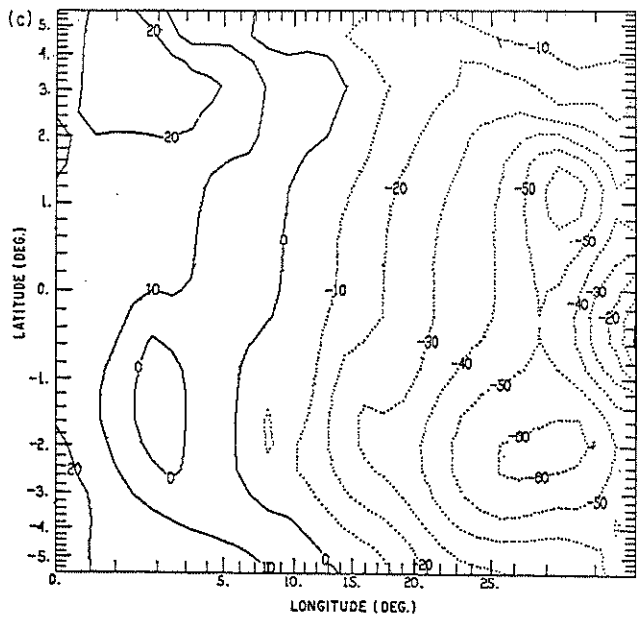

Figure 22. Nonlinear response to a southeasterly wind at day 40. Like Fig. 18 (a) u^0 (b) u^1 (c) h. Contour interval is 10 m.

state which resulted after 384 days; it is barely distinguishable from the one at day 398 depicted in Fig. 12.) At $t = 0$ a southerly wind component is added to the prevailing easterly component so that each wind component is .465 dynes cm^{-2}. This is intended to be a very crude analog of the southeast monsoon that occurs in the Atlantic in the late Spring. The linear response to a southeast wind is simply a superposition of the linear responses to a south wind and to an east wind but the nonlinear response is more complex.

The evolution of model energies, Figure 20, shows that after 400 days the model ocean still has not reached a truly steady state, even in the equatorial region. (The continued increase in PE and KE_1 appears to be due to a strengthening of the current at 4.5N. See Figure 22.) After day 80 the potential and upper layer kinetic energy do not vary greatly. The lower layer kinetic energy takes about twice as long to become approximately constant. In the equatorial region only the upper layer kinetic energy is substantially different from its value at $t = 0$.

Figure 21 is a plot of contours of u^1 at the equator with time as the ordinate. It is similar to Figure 17, which showed a regular progression of phase for the wave-like instability that arose in that south wind case. In the present case, in the time period from about day 25 to about day 175 there is some *apparent* phase propagation to

the west. However, none of the lines of constant amplitude cross the basin, and after day 175 all such east to west movement ceases. The pattern of evolution resembles the way in which the mixed mode in the linear south wind case contracts toward the western boundary with time (due to its Bessel function behavior; cf. CSII). We will return to this point after considering the early evolution of the flow.

The two most prominent developments in the first 40 days (see Fig. 22) are the southward shift of the undercurrent and the development of an eastward current between 3N and 5N. The latter resembles the south wind response, Sec. 7. The southward shifting of the undercurrent is already evident at 8 days. At the same time the surface currents near the equator have become westward. This upwind shifting of the undercurrent in the presence of meridional winds has been found in earlier theoretical investigations (Robinson, 1966; Charney and Spiegel, 1971) and has been observed in the world's oceans (e.g., Taft and Knauss, 1967).

The surface flow (Fig. 22a) strongly resembles the south wind response (Fig. 18a). The east wind influence shows most clearly in the poleward wind drift currents south of 1S. The lower layer currents (Fig. 22b) show effects from both the south wind (cf., Fig. 18b) and the east wind (cf., Fig. 12b displaced south). The region of eastward flow centered at about 1S is broader than is the case with either of the simpler wind systems. The eastward currents at 4N induced by the southerly wind component appeared first at the western side of the basin and gradually extended to the east. The layer depth still resembles its initial state (Fig. 12c) far more than the south wind response (Fig. 18c).

Between day 8 and day 40 the most important feature to appear in the lower layer is the wavy pattern which causes the undercurrent to meander about its mean latitude of about 0.6S. These meanders persist thereafter though their form changes. The disturbance propagates from west to east in the sense that it appears earlier at the western side. Figure 21 showed that any phase propagation is westward, but to speak of phase propagation is misleading. The meander pattern migrates westward over the first 175 days and then remains stationary. The result might be described as a standing wave of zero frequency. The structure of these meanders is most clearly revealed by the contours of the zonal and meridional transports at day 398 shown in Figure 23. They have their largest amplitude between 0 and 2S; with the amplitude decreasing from west to east. The wavelength of the meanders is about 650 km and shows a slight increase from west to east. We offer the interpretation that these meanders are due to a mode generated at the western boundary in response to the south wind. Such a mode is the nonlinear analog of the mixed mode that is generated when the initial state is a resting one. It plays the role of a barotropic instability in the sense of acting to reduce the horizontal shear of the zonal currents.

In addition to these meanders, the other prominent features of the flow in the equatorial region at day 398 are the eastward jet in both layers centered at 4N and

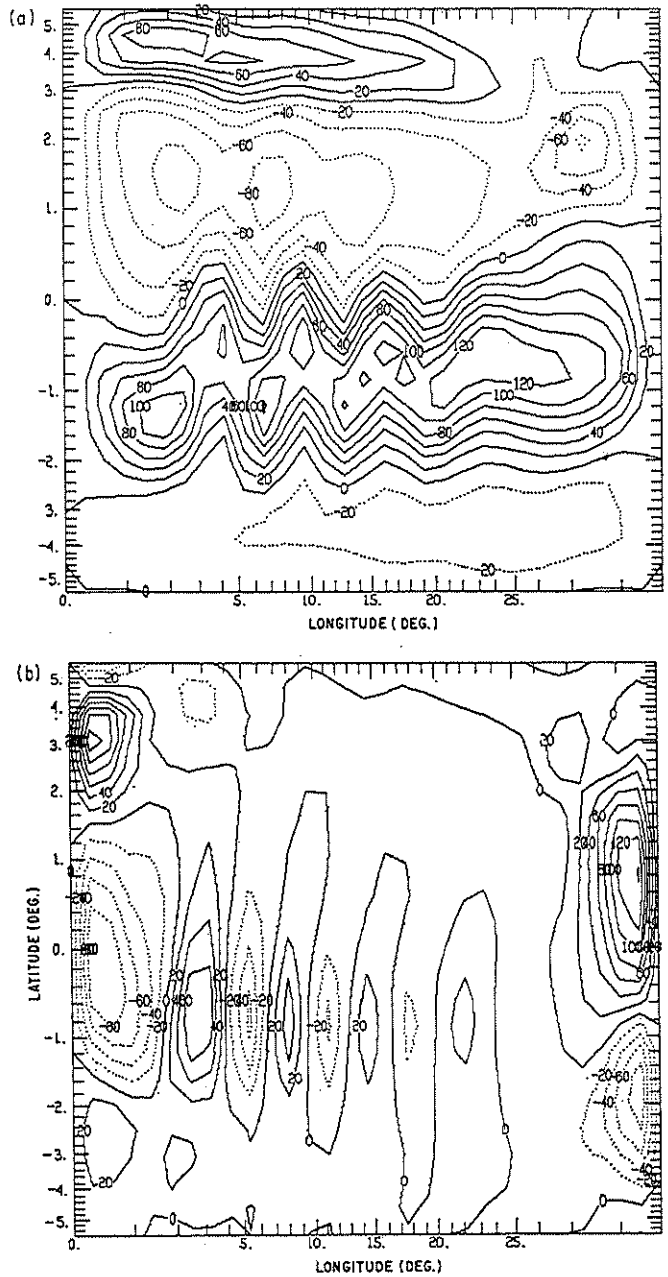

Figure 23. Contours of the vertically integrated transports in the nonlinear response to a southeasterly wind at day 398. Contour interval is 20 m^2 sec^{-1} (a) Zonal transport, $\bar{u}$. (b) Meridional transport, $\bar{v}$.

the undercurrent with a mean position at about 0.7S. Elsewhere between ±5° the lower layer currents are generally westward. Except that the jet is slightly further north and its total transport less than in the south wind case, the mean flow between the equator and about 5N is very similar in the two cases. The dynamical arguments presented in Sec. 7 apply here as well. South of the equator the two cases are quite different due to the presence of the undercurrent at about 1S and an additional region of westward transport to the south of it. The flow pattern between 3S and 3N that we find at day 398 resembles the similar calculation made by Charney and Spiegel (1971). (See their Figs. 9 and 10; they only show the region from 3S to 3N.) Flow in the meridional plane is similar in the two calculations, with the division between northward and southward surface flow occurring at the latitude of the undercurrent. Of course, since their model has no zonal variation, the meanders are absent.

9. Discussion

Timescales. The analysis in I showed that there are two timescales governing the flow. The first of these is the time for the transfer of wind energy to the upper frictional (Ekman) layer; this is 0 (20 days) in all cases. The second is the time for the sea surface to set up and establish the basin-wide pressure gradients. Away from the equator this setup time is that given by the linear analysis because the extra-equatorial dynamics are linear. (From our viewpoint the nonlinearities of the western boundary current region are a local effect that does not influence the large scale adjustment.) The setup time [0(1 year) at 10°] decreases toward low latitudes with the equatorial time varying greatly from case to case. Nonlinear effects may either lengthen or shorten the corresponding linear response time, with the result that the nonlinear time varies between 150 and 300 days. This setup time varies linearly with the longitudinal extent of the basin (for zonal winds, see below). The overall setup time for each of the world's equatorial oceans is thus longer than or comparable to the characteristic time for the major wind stress variations associated with the seasonal cycle. The oceans do not have enough time to adjust to be in equilibrium with the winds (eg. Sverdrup balance).

On the other hand, important features of the equatorial circulation are qualitatively present quite early. In all the zonal wind cases there is a significant zonal pressure gradient everywhere on the equator at 15 days, the time when the effects of the meridional boundaries are first felt at all longitudes. This occurs when the initial Kelvin and $n = 1$ Rossby modes meet. Nondimensionally this time is $3/4T$ where T is the time for a Kelvin wave to cross the basin. For the Indian and Atlantic Oceans the time T is approximately one month while for the Pacific it is three months, so boundary responses to seasonal variations have time to extend across each ocean. Another important milestone occurs at a time $4T$ (80 days in the experiments) when the first reflections (i.e., the $n = 1$ Rossby reflection of the initial Kelvin mode and the Kelvin reflection of the initial $n = 1$ Rossby mode) cross the basin. By this time enough of the zonal rearrangement of mass has been accomplished so that the circulation qualitatively resembles the steady state. If anything, the time $4T$ is more significant in the nonlinear cases because the nonlinearities tend to damp subsequent oscillations, especially with easterly winds. To the extent that the flow at this time is in equilibrium with the winds the Atlantic and Indian Oceans will be in equilibrium with the annual component of the winds and the Pacific will not.

Nonlinearity and waves. In all cases it is the surface flow on (and near) the equator that first becomes nonlinear; this occurs within three or four days (using a local Rossby number as a measure). Within two weeks nonlinear distortions of the flow field are evident in both layers. Vertical velocities are large and vertical advections play an important role in the lower layer circulation.

While the response to zonal winds involves both wave dynamics and nonlinear currents, the southerly wind response (with both resting and east wind initial states) is fundamentally nonlinear and wave concepts are inapplicable. It bears little resemblance to its linear counterpart and the setup time is unrelated to that given by linear theory. Adjustment occurs primarily in the meridional plane so the setup time is largely independent of the longitudinal extent of the ocean. Our results show that in the first month the ocean rapidly approaches its equilibrium value, changing only gradually thereafter (at least until the onset of instability). Since the real oceans are not initially at rest their response times to seasonal variations may differ somewhat from those given above. However, the setup time for a southerly wind was about the same for an initial state with an undercurrent and one at rest.

Undercurrent dynamics: easterlies and westerlies. We have seen that the model's response to easterlies (the prevailing winds in the equatorial Atlantic and Pacific) is rather different than its response to westerlies (as are present in the Indian Ocean with the onset of the southwest monsoon; see Wyrtki, 1973 and Knox, 1976). In the case of easterlies the undercurrent requires an eastward pressure gradient, not only as a direct driving, but also to produce equatorward flow. This undercurrent is nonlocal in character. It becomes established at a given longitude only when the meridional boundaries are felt there.

By contrast, the eastward flow at depth in response to westerlies is locally determined. The dynamics are frictional and inertial, relying upon frictionally induced surface convergence and associated downwelling to produce eastward momentum at depth. Because the response is local it is also quite rapid: within a week the undercurrent is nearly at full strength. The data collected by Knox (1976) at Gan is strong evidence for the rapid generation of an undercurrent after the onset of westerlies.

These observations also show that the currents reverse when the winds slacken or become meridional. Knox attributed this to westward flow driven by the pile up of

water at the eastern side, as in O'Brien and Hurlburt's (1974) numerical calculation. The same feature is present in our *linear* zonal wind response (cf. Sec. 3 and Fig 4) and was attributed to the eastern boundary Rossby waves overbalancing the wind stress. However, the transit time from the eastern boundary to Gan for such waves is not consistent with the observations [at least for the first baroclinic mode; but cf. Philander (1978b)]. Such a current reversal is not present in our *nonlinear* calculation where the pressure gradient slows the inertial eastward flow but is not strong enough to reverse it. Our model results suggest another explanation. Since the subsurface eastward flow is driven by local winds, the cessation of the wind eliminates the source of eastward momentum and the undercurrent can disappear as rapidly as it appeared. The basin-wide westward pressure gradient previously set up by the westerlies led to subsurface poleward flow which can now act to carry eastward momentum away from the equator. At the same time right on the equator it will drive a down gradient flow to the west. In addition, the calculation of Sec. 7 suggests that flow at the equator will be westward in the presence of meridional winds. (This is true whether the winds are northerly or southerly). Knox's observations are not inconsistent with this, but since the dynamics involve the equatorward advections of both surface and subsurface currents some knowledge of the currents off the equator is needed to decide whether this applies.

Downstream variations in the undercurrent. Our undercurrent calculation resembles the observed undercurrent in many important respects. It also shares many features with the x-independent model of Charney and Spiegel (1971), but permitting zonal variations and not constraining the pressure force to balance the zonal wind stress makes for some important differences. The pressure gradient was larger in our model, making it more in line with observational evidence (Montgomery and Palmen, 1940; also see Charney, 1960, p. 305). The terms uu_x and vu_y are of comparable magnitude. Previous theoretical studies of the undercurrent in homogeneous oceans have neglected the former term by arguing that the zonal length scale is much greater than the meridional one. However, in the undercurrent $u>>v$, so this argument breaks down. We have shown that either zonal variations or friction terms must enter the undercurrent momentum balance. For reasonable values of the coefficients of eddy viscosity and realistic basin sizes, zonal variations will enter before additional friction terms. (Observational accounts of the momentum balance in the undercurrent [Knauss, 1966; Taft, *et al.*, 1974) have also neglected downstream advections, but this is due primarily to a lack of data.]

The model results show an increase in transport downstream. Such behavior is observed in the western Pacific where the depth of the thermocline shows little variation (as is the case with the model's thermocline). In the eastern Atlantic and Pacific, where the thermocline becomes very shallow, undercurrent transports appear to decrease downstream. To reproduce this feature it appears to be necessary to include

some physical mechanism which allows the pressure gradient force to be uncoupled from the vertical extent of the undercurrent. One such possibility is the equatorial effect of the thermohaline circulation (Philander, 1973), though it may be enough for the model to allow downwelling beneath the undercurrent core. Observational evidence does not enable one to determine with certainty if the loss of fluid from the undercurrent occurs in the meridional or the vertical plane.

Countercurrent dynamics. Sverdrup's (1947) explanation of the relationship between the North Equatorial Countercurrent and the curl of the wind stress is one of the great triumphs of dynamical oceanography. Studies based on more recent observational data (Kendall, 1970) have shown some discrepancies from the Sverdrup balance. The model results in the southerly and southeasterly wind cases suggest a possible cause for these discrepancies. In both of these cases a strong eastward jet developed in both model layers as a response to the southerly wind component. In the pure south wind case this jet is centered at 3N; with southeasterlies it is at 4N. In both cases it extends to 5N and so would overlap the wind stress curl driven countercurrent at its southern edge. The evolution of this countercurrent was explained in terms of the kinematic effects of advection on the linear response in the frictional surface layer. A simple argument based on conservation of vorticity and energy was given to explain the steady state flow pattern. This analysis shows that the velocity of the eastward jet varies as $\tau^{2/3}$ (τ is the meridional wind stress), and that its latitude varies as $\tau^{1/3}$ and so is relatively insensitive to the wind speed.

While we believe the dynamics discussed above are important to a thorough description of the countercurrents in the Atlantic and Pacific Oceans, they appear to play a more fundamental role in explaining the flow pattern observed in the equatorial Indian Ocean. Observations in the western Indian Ocean during the southwest monsoon (Taft and Knauss, 1967, Nederlands Meteorologisch Instituut, 1952) have shown weak eastward flow extending north of the equator and then giving way to westward currents that have a maximum at 3N (cf. Fig. 18). During the northerly wind regime (i.e. the northwest monsoon) the reverse pattern is observed over the central Indian Ocean, with westward currents south of the equator.

Stability. The zonal wind cases showed no evidence of instability (e.g., meanders of the undercurrent) whatsoever. The current system associated with a south wind was seen to be barotropically unstable, the instability having a regular wavelike form in the zonal direction with a wavelength of 950 km and a period of 29 days. The interpretation of the standing wave pattern which arises in the southeast wind case is less straightforward. It appears that by absorbing energy from the mean flow the initial western boundary reflection maintains its amplitude at all longitudes. This contrasts with the linear response, in which this Bessel function shaped mode collapses toward the western side.

These results are in agreement with the finding of Philanders's (1976, 1978a) stability studies: the undercurrent itself is stable but the entire equatorial current-countercurrent system may be unstable—in particular, because of the large shears between the westward flow near the equator and the eastward flow in the North Equatorial Countercurrent. This instability is the probable source of the waves observed on the front between the Countercurrent and the South Equatorial Current in the Pacific (Legeckis, 1977). Those waves have a wavelength of about 1000 km and 25 day period.

The southeast case has an undercurrent which meanders in space but is steady in time. In the course of reaching this steady state, the undercurrent exhibited time variations not unlike those observed during GATE (Düing *et al.*, 1975). Rather than being an instability, it is possible that the observed meanders are part of the ocean's adjustment to changes in the wind (cf Hallock, 1977), though the data record is too short to be conclusive.

Acknowledgments. I am grateful to my advisor, Professor J. G. Charney, for his guidance and encouragement. Several valuable conversations with Professor H. M. Stommel are acknowledged. Professors Eugenia Rivas and Moshe Israeli provided much useful advice about numerical methods. My special thanks to Dr. E. S. Sarachik, for providing invaluable criticisms throughout the course of this work.

The computations were carried out at the Goddard Institute for Space Studies. My thanks to Dr. Robert Jastrow and Dr. Milton Halem for making this possible. This work was supported by NASA Grant NGR 22-009727 to the Massachusetts Institute of Technology.

REFERENCES

Cane, M. A. 1975. A study of the wind-driven ocean circulation in an equatorial basin, Ph.D. thesis, Massachusetts Institute of Technology, 372 pp.

—— 1977. The response of an equatorial ocean to simple wind stress patterns: I. Model formulation and analytic results. J. Mar. Res., *37,* 233–252.

Cane, M. A. and E. S. Sarachik. 1976. Forced baroclinic ocean motions: I. The linear equatorial unbounded case. J. Mar. Res., *34,* 629–665.

—— 1977. Forced baroclinic ocean motions: II. The linear equatorial bounded case. J. Mar. Res., *35,* 395–432.

—— 1979. Forced baroclinic ocean motions: III. The linear basin case. J. Mar. Res., *37* (this issue).

Charney, J. G. 1955. The generation of ocean currents by wind. J. Mar. Res., *14,* 477–498.

—— 1960. Non-linear theory of a wind-driven homogeneous layer near the equator. Deep Sea Res., *6,* 303–310.

Charney, J. G. and S. Spiegel. 1971. Structure of wind driven equatorial currents in homogeneous oceans. J. Phys. Oceanogr., *1,* 149–160.

Düing, W., P. Hisard, E. Katz, J. Krauss, J. Meincke, K. Moroshkin, G. Philander, A. Rybnikov, and K. Voigt. 1975. Meanders and long waves in the Equatorial Atlantic. Nature, *257,* 280–284.

Fofonoff, N. P. and R. B. Montgomery. 1955. The equatorial undercurrent in the light of the vorticity equation. Tellus, *7,* 518–521.

Hallock, Z. R. 1977. Wind forced equatorial waves in the Atlantic Ocean. Ph.D. Thesis, University of Miami.

Kendall, T. R. 1970. The Pacific Equatorial Countercurrent. International Center for Environmental Research, Laguna Beach, CA., 19 pp.

Knauss, J. A. 1966. Further measurements and observations on the Cromwell Current. J. Mar. Res., *24,* 205–240.

Knox, R. A. 1976. On a long series of measurement of Indian Ocean equatorial currents near Addu Atoll. Deep Sea Res., *23,* 211–221.

Legeckis, R. 1977. Long waves in the eastern equatorial Pacific; a view from a geostationary satellite. Science, *197,* 1179–1181.

Lorenz, E. N. 1971. An N-cycle time-differencing scheme for stepwise numerical integration. Mon. Wea. Rev., *99,* 644–648.

Mesinger, F. 1972. A method for construction of second-order accuracy difference schemes permitting no false two-grid interval wave in the height field. Tellus, *XXV,* 444–457.

Montgomery, R. B. and Palmen, E. 1940. Contribution to the question of the Equatorial Counter Current. J. Mar. Res., *3,* 112–133.

Nederlands Meteorologisch Instituut, 1952. Indische Ocean oceanografische'en meteorologische gegevens. Publ. no. 135, 2nd ed., *Vol. 1,* 31 pp., *Vol. 2,* 24 charts.

O'Brien, J. J. and H. E. Hurlburt. 1974. Equatorial jet in the Indian Ocean: Theory. Science, *184,* 1075–1077.

Orszag, S. and M. Israeli. 1974. Numerical simulation of viscous incompressible flows, *in* Annual Review of Fluid Mechanics, *Vol. 6,* Palo Alto, Annual Reviews, 371 pp.

Philander, S. G. H. 1971. The equatorial dynamics of a shallow homogeneous ocean. Geophys. Fluid Dyn., *2,* 219–245.

—— 1973. The equatorial thermocline. Deep Sea Res., *20,* 69–86.

—— 1976. Instabilities of zonal equatorial currents. J. Geophys. Res., *81,* 3725–3735.

—— 1978a. Instabilities of zonal equatorial currents: II. J. Geophys. Res., submitted.

—— 1978b. Variability of the tropical oceans Dyn. Atmos. Oceans, submitted.

Robinson, A. R. 1966. An investigation into the wind as the cause of the Equatorial Undercurrent. J. Mar. Res., *24,* 179–204.

Taft, B. A. and J .A. Knauss. 1967. The Equatorial Undercurrent of the Indian Ocean as observed by the Lusiad expedition. Bull. Scripps Inst. Oceanogr., *9.*

Taft, B. A., B. Hickey, C. Wunsch and D. Baker. 1974. The Cromwell Current at 150°W. Deep Sea Res., *21,* 403–430.

Wyrtki, K. 1973. An equatorial jet in the Indian Ocean. Science, *181,* 262–264.

Received: *17 June, 1977;* revised: *22 November, 1978.*